Clouds as Seen by Satellite Sounders (3I) and Imagers (ISCCP). Part III: Spatial Heterogeneity and Radiative Effects

C. J. STUBENRAUCH

Laboratoire de Météorologie Dynamique, Ecole Polytechnique, Palaiseau, France

W. B. ROSSOW

Institute for Space Studies, NASA/Goddard Space Flight Center, New York, New York

N. A. SCOTT AND A. CHÉDIN

Laboratoire de Météorologie Dynamique, Ecole Polytechnique, Palaiseau, France

(Manuscript received 20 January 1998, in final form 11 November 1998)

ABSTRACT

Their relatively good spectral resolution makes infrared sounders very useful for the determination of cloud properties (day and night), and their coarse spatial resolution has less effect on clouds with large spatial extents like cirrus clouds. The Improved Initialization Inversion (3I) algorithms convert TIROS-N Operational Vertical Sounder observations from the NOAA Polar Orbiting Environmental Satellites into atmospheric temperature and humidity profiles and into cloud and surface properties. On the other hand, the relatively high spatial resolution of the imagers from the geostationary and polar orbiting satellites used in the International Satellite Cloud Climatology Project (ISCCP) is important for the determination of properties of clouds with smaller spatial extents like boundary layer clouds. By combining these quite different datasets some insight into the behavior of retrieved cloud properties with spatial heterogeneity is gained. The effective cloud amount as determined by 3I and ISCCP agrees very well for homogeneous cloud types at all heights, but heterogeneous cloud scenes lead to a smaller 3I effective cloud amount than the one retrieved by ISCCP. In the case of thin cirrus overlying low clouds, 3I will determine the effective cloud amount of the cirrus, whereas ISCCP's information from the visible channel includes the lower cloud. The correlation between infrared cloud emissivity (3I) and visible cloud optical thickness (ISCCP) agrees quite well for high clouds with the expected exponential behavior. Mesoscale heterogeneities in midlevel and low-level cloud fields, however, cause a flatter behavior between 3I retrieved cloud emissivity and ISCCP retrieved cloud optical thickness, which can be simulated in a GCM with a subgrid-scale cloud overlapping scheme. Cloud radiative effects are studied in combination with Earth Radiation Budget Experiment fluxes. The warming effect of clouds depends on cloud height and effective cloud amount, but also on atmospheric conditions like near-surface temperature and humidity. The variability ranges from nearly no effect for partially covered low clouds up to 150 W m^{-2} for overcast high opaque clouds in the Tropics. The reprocessing of ISCCP produced a better distinction between the radiative effects of high opaque and cirrus clouds, in better agreement with the 3I results. Still, 3I high opaque clouds produce about 10 W m^{-2} larger warming. The cooling effect of clouds during the daytime depends very much on solar inclination as well as cloud optical thickness and cover.

1. Introduction

The low spatial resolution of climate general circulation models (about 100–500 km) makes the treatment of clouds in their radiative flux calculations dependent on assumptions about the importance and effect of smaller-scale cloud heterogeneities. This is one of several reasons why the feedbacks of clouds on CO_2-increase-induced global climate warming predictions by these models are so uncertain. To improve the situation, it is necessary to understand and describe more accurately the interaction between clouds and radiation that can be observed directly. By combining cloud properties determined by the Improved Initialization Inversion (3I) analysis (Chédin et al. 1985; Scott et al. 1999) of satellite infrared sounder data and the International Sat-

Corresponding author address: Dr. C. J. Stubenrauch, Laboratoire de Meteorologie Dynamique, Ecole Polytechnique, 91128 Palaiseau Cedex, France.
E-mail: stubenrauch@lmd.polytechnique.fr

ellite Cloud Climatology Project (ISCCP) analysis (Rossow and Schiffer 1991, Rossow et al. 1996) of satellite imager data with Earth Radiation Budget Experiment (ERBE) determinations of radiative fluxes at the top of the atmosphere (TOA), one can study the effects of smaller-scale cloud variations on radiation by exploiting differences in spectral and spatial resolution.

Both ISCCP and 3I provide global cloud climatologies. For climate studies, using one of these datasets, it is important to understand how cloud properties are perceived by these different instruments and inversion methods. Within the framework of the National Oceanic and Atmospheric Administration–National Aeronautics and Space Administration (NOAA–NASA) Pathfinder program (M. Maiden et al. 1994, personal communication), eight years of TIROS-N (Television Infrared Observation Satellite) Operational Vertical Sounder (TOVS) data (*NOAA-10* and *NOAA-12*) have already been processed by the 3I algorithms, using a weighted-χ^2 method for cloud parameter determination (Stubenrauch et al. 1999a). The data processing is presently going on (*NOAA-11*) at the rate of two months of data per day, providing atmospheric temperature and water vapor profiles as well as cloud and surface parameters at a spatial resolution of 1°. Results for the whole TOVS observation period from 1979 until now should be available in 2000, depending on progress on recalibration of the High-Resolution Infrared Sounder (HIRS) brightness temperatures obtained by comparing airmass-averaged brightness temperatures computed from radiosonde measurements to collocated observed brightness temperatures (Armante et al. 1998). ISCCP has reprocessed 11 years of data (D series); the whole dataset, covering 1983 until now, should be available early in 2000.

After the evaluation of the 3I and ISCCP cloud properties in Stubenrauch et al. (1999c), we discuss in this article the effect of spatial heterogeneity on the determination of these cloud properties and on their correlations. The spatial heterogeneity effect on cloudy radiation is also studied with time–space collocated radiative fluxes determined by ERBE.

The 3I and ISCCP methods of cloud parameter determination have been thoroughly described (Stubenrauch et al. 1999c and 1999a, henceforth Parts I and II); the most important differences are briefly summarized in section 2. The collocation of the ERBE data with the 3I and ISCCP results is also described in section 2. We study the effect of spatial heterogeneity on the satellite retrieval of cloud properties and on correlations between optical and thermal cloud properties in section 3. For this study we use some of the same geographical regions selected in Fig. 11 of Part I. In section 4, we investigate differences in ERBE radiative TOA fluxes assigned to the different cloud types and cloud properties as determined by 3I and by ISCCP. Conclusions are drawn in section 5.

2. Methods and datasets

a. 3I and ISCCP cloud parameter determination

The High-Resolution Infrared Sounder instrument, which is part of the TOVS system (Smith et al. 1979), measures radiation emitted and scattered from different levels of the atmosphere at 19 infrared (IR) wavelengths as well as one visible (VIS) wavelength. The 3I algorithms transform these radiances into atmospheric, cloud, and surface properties using a fast line-by-line radiative transfer model, Automatized Atmospheric Absorption Atlas, and a huge collection of radiosonde measurements of temperature, humidity, and pressure that are grouped by atmospheric conditions: the Thermodynamic Initial Guess Retrieval dataset.

The basis for cloud detection at HIRS spatial resolution (17 km at nadir) is the use of simultaneous Microwave Sounding Unit radiance measurements. Since the latter probe through the clouds, they are used to predict clear sky IR brightness temperatures, which are compared to those of the HIRS instrument for all individual pixels to decide if they are cloudy. A summary of the 3I cloud detection scheme is given in Table 1 of Part I.

To reduce time-consuming calculations, the HIRS radiances are averaged separately over clear pixels and over cloudy pixels within 100 km × 100 km regions. At this spatial resolution we distinguish three situations: 1) clear sky—all pixels are clear and no cloud parameters are determined; 2) partly cloudy—clear pixels are used for temperature and water vapor profile determination, and cloudy pixels for cloud parameter determination; and 3) overcast—all pixels are cloudy. In case 3 all pixels are used to compute cloud parameters and clear radiances are inferred from the warmest homogenous pixels (under the hypothesis that these correspond to partially cloud covered pixels) by the ''ψ method'' (Chédin et al. 1985) for temperature inversion and by using the effective cloud amount for water vapor inversion (Chaboureau et al. 1998). The atmospheric and surface properties are then determined from the clear (or ''cloud cleared'') radiances.

Cloud parameters are determined from the *averaged cloudy pixel radiances* assuming that all cloudy pixels are covered by a *single homogeneous cloud layer*. The average cloud-top pressure, $p_{\rm cld}$, and the average effective cloud emissivity over these cloudy pixels, $N\varepsilon_{\rm cld}$, are obtained by a ''weighted χ^2'' method using four radiances in the 15-μm CO_2 band (HIRS channel numbers 4–7, with peak responses from 400- to 900-hPa levels in the atmosphere) and in the 11-μm IR atmospheric window (HIRS channel number 8): Minimizing χ^2_w in Eq. (1) is equivalent to $d\chi^2_w/dN\varepsilon_{\rm cld}(p_k) = 0$, from which one can extract $N\varepsilon_{\rm cld}(p_k)$ [Eq. (5) in Part II]. Calculations of $N\varepsilon_{\rm cld}(p_k)$ at 30 cloud pressure levels k are searched to choose the solution with the minimum χ^2_w:

$$\chi^2_w(p_k) = \sum_{i=4}^{8} \frac{\{[I_{\rm cld}(p_k, \nu_i) - I_{\rm clr}(\nu_i)]N\varepsilon_{\rm cld}(p_k) - [I_m(\nu_i) - I_{\rm clr}(\nu_i)]\}^2}{\sigma^2(\nu_i)} W^2(p_k, \nu_i), \quad (1)$$

where the measured radiance is I_m, the retrieved clear sky radiance is $I_{\rm clr}$ at the frequency ν_i of HIRS channel i, and the calculated radiance emitted by a homogeneous opaque single cloud layer at pressure level k is $I_{\rm cld}$. The empirical weights $W^2(p_k, \nu_i)$, depending on cloud pressure level k and frequency ν_i, take into account the weighting functions of the different channels as well as the effect of temperature profile uncertainties on the difference between clear sky and cloudy radiances $I_{\rm clr}(\nu_i) - I_{\rm cld}(p_k, \nu_i)$. Also, $\sigma(\nu_i)$ corresponds to the instrument noise, which is assumed to be channel independent, as in Eyre and Menzel (1989). The method and the determination of the empirical weights are described in detail in Part II.

In the 3I cloud algorithm, the spectrally averaged emissivity over cloudy HIRS pixels is called ''effective cloud emissivity'' $N\varepsilon_{\rm cld}$, because pixels identified as cloudy may in reality be partly cloudy due to the coarse spatial resolution of the HIRS pixels. Pathfinder data have been organized on a 1° latitude × 1° longitude grid. We also determine a cloud cover fraction ''cov'' as the fraction of the total number of pixels, $N_{\rm tot}$, in each 1° grid that are cloudy:

$$\text{cov} = N_{\rm cld}/N_{\rm tot}. \quad (2)$$

Thus, the effective cloud amount over a 1° grid, henceforth called ''εN,'' is the product of cloud cover fraction and effective cloud emissivity for the cloudy pixels, $N\varepsilon_{\rm cld}$:

$$\varepsilon N = \text{cov} \times N\varepsilon_{\rm cld}. \quad (3)$$

Cloud types are defined by the cloud-top pressure and effective cloud amount. High clouds ($p_{\rm cld} < 440$ hPa) are divided into three categories: opaque ($N\varepsilon_{\rm cld} > 90\%$), cirrus ($90\% < N\varepsilon_{\rm cld} < 50\%$), or thin cirrus ($N\varepsilon_{\rm cld} < 50\%$). Since midlevel (440 h Pa $< p_{\rm cld} < 680$ hPa) and low-level ($p_{\rm cld} > 680$ hPa) clouds have a smaller horizontal extension, only two classes in each height category can be distinguished: mostly cloudy or overcast ($\varepsilon N > 50\%$) and partly cloudy ($\varepsilon N < 50\%$) fields. The cloud types are summarized in Table 2 of Part I.

For its global cloud climatology, ISCCP put emphasis on temporal and spatial resolution, rather than on spectral resolution, by using one visible (day only) and one IR atmospheric window radiance measurement from imagers on the suite of geostationary and polar orbiting weather satellites. Time sampling is three hourly and the initial spatial resolution of about 5 km is sampled to intervals of about 30 km, which means that about 1 pixel out of 36 is kept for cloud information. Clouds are detected through an IR–VIS threshold test that compares the measured radiances to clear sky composite radiances that have been inferred from a series of statistical tests on the space and time variations of the IR and VIS radiances (Rossow et al. 1993). Clear sky conditions are associated with low IR and VIS spatial and temporal variability.

ISCCP cloud properties are determined for each pixel by comparing the observed radiances with a detailed radiative transfer model. The model includes the effects of the atmosphere, with properties specified from the operational analysis of the TOVS data (only one profile per day is available), and surface determined from the clear radiances. Cloudy pixels are assumed to be covered completely by a single homogeneous cloud layer, but this time over a region of 5 km × 5 km. Cloud-top temperature, $T_{\rm cld}$, is first retrieved assuming that all clouds are blackbodies. During daytime, when VIS radiances can be used to retrieve cloud optical thicknesses, τ, the cloud-top temperature of ''transmissive'' clouds ($\tau_{\rm IR} < 5.5$) is corrected to account for the radiation transmitted from below; $T_{\rm cld}$ is decreased as a function of τ. In the first version of the ISCCP data (called CX), all clouds were represented in the radiative model by a cloud composed of 10-μm-radius spherical liquid water droplets; in the new ISCCP dataset (called DX), clouds with $T_{\rm cld} \geq 260$ K are treated with the same liquid cloud model, but all clouds with $T_{\rm cld} < 260$ K are treated with a model cloud composed of 30-μm ice polycrystals (Rossow et al. 1996). Clouds are classified into nine types (only during day), according to three cloud-top pressure intervals (separated at 440 and 680 hPa) and three visible optical thickness intervals (divided at 3.6 and 23).

b. Collocation of 3I and ISCCP cloud parameters

The 3I cloud parameters (HIRS–MSU measurements) and ISCCP pixel data [Advanced Very High Resolution Radiometer (AVHRR) measurements)] from the same polar satellite *NOAA-10* (observations at ~0730 local time) have been combined into 1° latitude × 1° longitude grid boxes for July 1987 and January 1988. The ISCCP version of the AVHRR measurements samples the global area coverage format to intervals of about 25 km; the initial spatial resolution of 1 km deteriorated to about 1 km × 4 km by averaging four pixels in a line and sampling every fifth line. The data have been divided into morning (AM) and evening (PM) observations. Starting from the pixel observations allows a simultaneous collocated comparison and combined use of the different cloud information. The combination of the ISCCP dataset and the 3I cloud parameters provides full

information only during daylight conditions. During the night ISCCP has only 50% of its information available.

Due to the better spatial resolution of ISCCP, we determine the ISCCP cloud type over a 1° grid as the most frequent of the nine ISCCP cloud types inside the 1° grid; and, in addition, we can determine cloud-type heterogeneity (in optical thickness as well as in height) inside the 1° grid. ISCCP cloud cover is the fraction of cloudy ISCCP pixels inside a 1° grid. For a detailed comparison, we also transform the optical thickness retrieved by ISCCP, together with the cloud cover, into IR effective cloud amount over the 1° grid (see section 3).

c. ERBE observations

For the analysis of cloud radiative effects, broadband top-of-the-atmosphere fluxes (Barkstrom et al. 1989) from the ERBE S8 dataset (instantaneous pixel measurements, here taken from *NOAA-10*) at a spatial resolution of about 40 km at nadir have been averaged into 1° latitude × 1° longitude grid boxes and have been divided, like the 3I and ISCCP measurements, into AM and PM for the same time period. To ensure accurate spatial collocation, the ERBE coordinates, given at the top of the atmosphere, are transformed to surface coordinates, which are used in the cloud datasets. The coordinate transformation (Stubenrauch 1993), which depends on the satellite viewing angle, can make a difference of up to 2 W m^{-2} in the longwave (LW) and up to 10 W m^{-2} in the shortwave (SW) instantaneous fluxes averaged over 1° latitude and 1° longitude. The daytime LW radiances are obtained by subtracting the measured SW radiances from the total (0.2–100 μm) radiances. Hence, SW calibration and spectral correction problems in the original ERBE data produce an underestimated LW flux in the afternoon observations by *NOAA-9* and an overestimated LW flux in the morning observations by *NOAA-10* (Thomas et al. 1995). We have applied the correction suggested by Eq. (14) in Thomas et al. (1995), which consists of subtracting at pixel level the filtered SW radiance times 6.04 (a factor determined by regression for *NOAA-10*) from the daytime unfiltered LW radiance. This leads to a decrease of the *NOAA-10* LW fluxes by up to 8 W m^{-2} (for bright cold clouds).

At 0730 local time, reflected SW fluxes are quite difficult to determine because of the low elevation of the sun, requiring stronger (and more uncertain) angular corrections of the measured radiances. Nevertheless, we have tried to correlate reflected SW fluxes and outgoing LW fluxes under different conditions of cloud heterogeneity in section 4c for the summer (illuminated) hemisphere midlatitudes at 0730 LT.

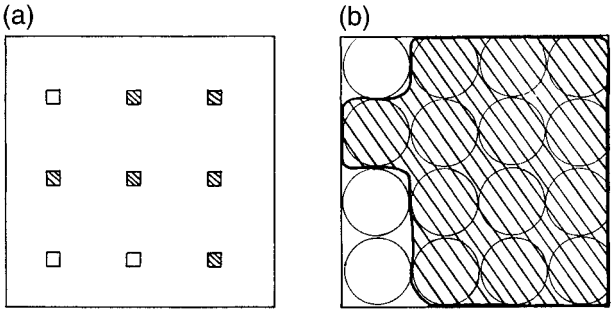

FIG. 1. Illustration of the spatial difference in ISCCP and 3I cloud observations. A 1° lat × 1° long grid box is filled (a) with approximately 1 km × 4 km large AVHRR pixels that are sampled every 35 km in satellite flight direction and every 30 km perpendicular to flight direction and (b) with approximately 20 km × 20 km large HIRS pixels. Pixels detected as cloudy are hatched, for one example situation. In the case of ISCCP, cloud parameters are determined from each of these sampled observations, whereas 3I cloud parameters are determined over the mean radiances over the whole cloudy region.

3. Heterogeneity effects on the determination of cloud properties

a. Effective cloud amount

Since 3I identifies cirrus during daytime as well as during nighttime, the 3I cloud parameters could be used to supplement the ISCCP results at nighttime for more complete diurnal cloud information. Therefore, one has first to study how to match the information of both cloud datasets quantitatively.

Using the collocated 3I–ISCCP cloud dataset, we study the effects of cloud spatial heterogeneity on the satellite retrievals of cloud properties caused by the different spatial resolutions of the radiance measurements (20 km and 5 km), different data volume reduction procedures (averaging and sampling), as well as different retrieval methods (multispectral IR and combination of VIS and IR). Figure 1 illustrates the different spatial coverages of the 3I and ISCCP cloud parameters. Variability within each 1° grid can arise because of partial coverage (broken cloudiness), because of horizontal heterogeneities of the optical and thermal properties of a cloud layer, and because of multilayer cloud structure. All of these effects should affect the 3I and ISCCP cloud parameters differently. The dominant form of heterogeneity should also be cloud-type dependent.

To test these effects, we consider high-, mid-, and low-level clouds, and for each cloud category, we distinguish three cases of cloud heterogeneity over each 1° grid: 1) a homogeneous cloud cover defined by ISCCP showing the same cloud type (see section 2a) for all cloudy pixels (called a homogeneous single-layer cloud), 2) ISCCP clouds all in the same height category but with larger optical thickness variations (called a heterogeneous single-layer cloud), and 3) ISCCP clouds with different heights and different optical thicknesses (called a multilayer cloud). Cloud-free grid boxes are eliminated for this analysis.

For the analysis of the cloud heterogeneity effect on the determination of the effective cloud amount over a 1° grid box, εN, we first have to transform the visible optical thickness, τ, retrieved by ISCCP into an IR cloud emissivity, ε, by using the following formula:

$$\varepsilon = 1 - \exp(-\tau/b), \quad (4)$$

where b relates the optical thickness from the VIS to that from the IR wavelength, depending on the cloud phase: $b = 2.13$ for ice clouds (Minnis et al. 1993) and $b = 2.56$ for water clouds (Rossow et al. 1996). These values of b do not account for IR scattering effects, which are very small except for very thin clouds (Rossow et al. 1996). The optical thickness, τ, of each cloudy ISCCP pixel within the 1° grid box has been transformed into an equivalent cloud emissivity, ε, by Eq. (4), and then these ε's have been averaged over the cloudy pixels within the 1° grid to $\overline{\varepsilon}$ [see appendix, Eq. (A2)]. This averaging method is compared in the appendix to two other methods of averaging that have been used before for averaging ISCCP measurements over 2.5° × 2.5° areas.

Finally, the averaged ISCCP IR cloud emissivity $\overline{\varepsilon}$ is multiplied by the ISCCP cloud cover fraction to obtain the effective cloud amount over a 1° grid.

Figures 2a–i show the normalized difference distributions between ISCCP and 3I effective cloud amount, separately for high- (panels a,d,g), mid- (panels b,e,h), and low-level (panels c,f,i) clouds *as identified by 3I*, under the three heterogeneity conditions explained above. Three different geographical regions are used for illustration: Northern Hemisphere midlatitude land (NL; Figs. 2a–c), Northern hemisphere midlatitude ocean (NH; Figs. 2d–f), and Southern Hemisphere midlatitude ocean (SH; Figs. 2g–i). These regions span the latitude band from 40° to 70°N and from 40° to 70°S, respectively. The difference distributions all peak around zero, but their tails are shifted more toward larger positive or negative values depending on cloud height and heterogeneity condition. The distribution widths stay about the same in each height category: For high clouds the standard deviation is about 0.2, increasing with decreasing cloud height class from about 0.25 for midlevel clouds to 0.30 for low-level clouds. This indicates mostly that low-level clouds are determined by 3I with higher noise.

Figures 3a (NL), 3b (NH), and 3c (SH) show the mean values of these distributions, separately over high-, mid-, and low-level clouds as identified by 3I, under the three heterogeneity conditions explained above. Since the peaks in Figs. 2a–i are all around zero, a difference in the mean value reflects a shift in the tails. From both figures we deduce that 1) in the case of a homogeneous single-layer cloud, εN determined by 3I and by ISCCP are on average about the same (within 5%), with a tendency of a lower εN from 3I than from ISCCP for homogeneous low clouds, which have a much smaller cloud cover (especially over NL) than the other cloud categories and therefore a much higher probability of partly covered HIRS pixels; 2) variability in optical thickness leads to an about 10% smaller εN determined by 3I (from averaged radiances) than εN determined by ISCCP (from sampled radiances) for all cloud height categories; and 3) in the case of multilayer clouds, the average εN calculated by 3I shifts to a value that is about 15% smaller for 3I high clouds than εN obtained by ISCCP, whereas for 3I low-level clouds there is no difference in εN. The second result arises, as we show below (see also appendix), mostly from the different effects of averaging on the different nonlinear relationships of reflectivity and emissivity with optical thickness.

This last result indicates that, in the case of thin cirrus clouds mixed with low- or midlevel clouds, which occur for about 25% of all clouds (Jin and Rossow 1997; Warren et al. 1985), the 3I result is dominated by the properties of the overlying cirrus clouds whereas the ISCCP result from the visible reflectivity includes the (usually larger) effective cloud amount of the thicker cloud underneath.

We have investigated these effects in two ways: First we changed the 3I algorithms to compute the cloud parameters for every individual cloudy HIRS pixel (keeping the same atmospheric temperature profiles) with cloud type per pixel determined from $N\varepsilon_{\mathrm{cld}}$ and from p_{cld} as described in section 2a. By comparing the retrieval once per 100 km × 100 km box (3I box) and once per HIRS pixel (3I pixel), we can look at the cloud-type distributions within the seven 3I cloud types determined from $N\varepsilon_{\mathrm{cld}}$ and p_{cld} computed once per box. Table 1 shows the percentage of 3I-pixel cloud types for each of the seven 3I-box cloud types described in section 2a over a tropical ocean region. One can see that thicker clouds, especially high opaque clouds and stratus clouds, seem to be the most concentrated (i.e., homogeneous) within a 1° grid (84% and 75%, respectively), whereas the thinner cloud types, especially thin cirrus and altocumulus, are more often seen in combination with other cloud types. Such cloud-type associations are qualitively similar to those found by comparing ISCCP and surface cloud observations. Note that 3I boxes identified as thin cirrus include 21% of stratus clouds, confirming the ISCCP–3I εN difference explanation above for multilayer high clouds. The difference between the box-averaged $N\varepsilon_{\mathrm{cld}}$ obtained over each pixel and $N\varepsilon_{\mathrm{cld}}$ obtained from average cloudy radiances over the box is, on average, zero over the whole studied region.

In Fig. 4 heterogeneity effects are examined again, separately for high-, mid-, and low-level clouds. If all HIRS pixels are covered by the same 3I cloud type, the $N\varepsilon_{\mathrm{cld}}$ difference is on average zero as expected. Horizontal heterogeneities within one cloud height type seem to effect mostly midlevel clouds. In the case of multilevel clouds, the mean $N\varepsilon_{\mathrm{cld}}$ calculated per HIRS pixel is much higher (about 20%) than $N\varepsilon_{\mathrm{cld}}$ obtained from

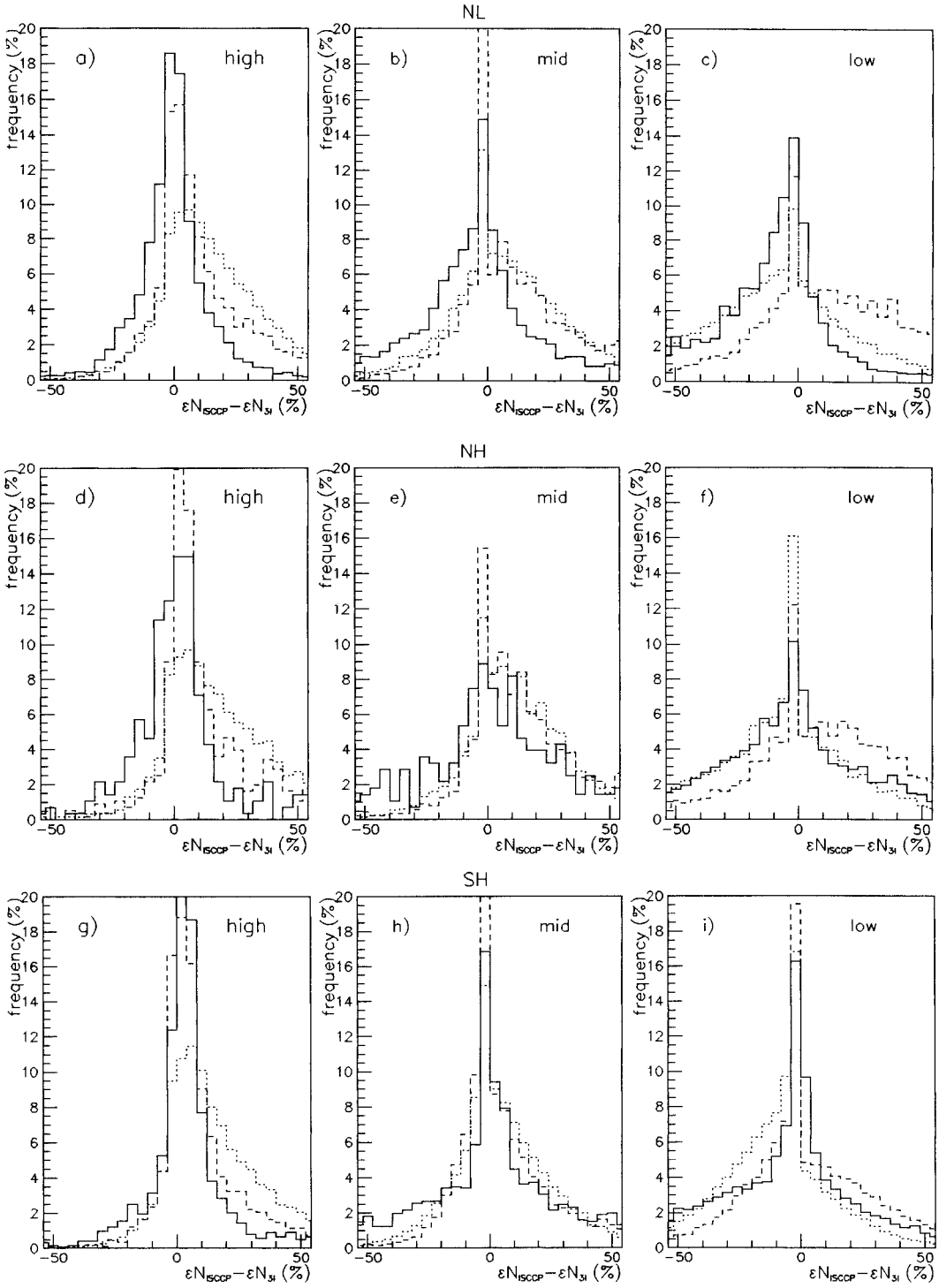

FIG. 2. Monthly mean distributions of the difference between effective cloud amounts, εN, determined by ISCCP and by 3I at 1° spatial resolution. Three geographical regions, under sun illumination (in summer), are considered: (a)–(c) Northern Hemisphere midlatitude land (NI), (d)–(f) North Atlantic (NA), and (g)–(i) Southern Hemisphere midlatitude ocean (SH). Distributions are shown separately for high- (a), (d), (g), mid- (b), (e), (h), and low-level (c), (f), (i) clouds as identified by 3I. In each figure, distributions are compared for three spatial heterogeneity situations as distinguished by ISCCP: homogeneous single-layer cloud (———, same ISCCP cloud type over 1° grid), heterogeneous single-layer cloud (– – –, same ISCCP cloud height but heterogeneous τ), and multilayer clouds (·····, different ISCCP cloud heights and τ).

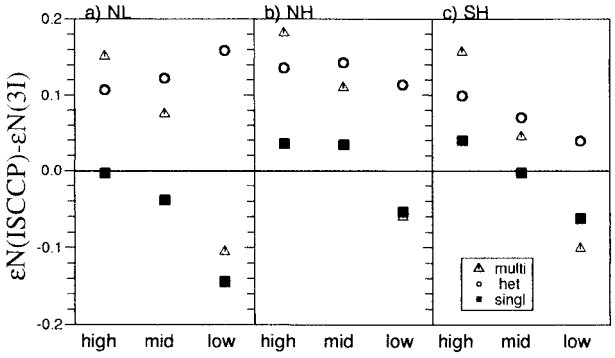

FIG. 3. Monthly mean values of the difference between εN determined by ISCCP and by 3I at 1° spatial resolution for high-, mid-, and low-level clouds as identified by 3I. Three geographical regions, under sun illumination (in summer), are considered: (a) NL, (b) NH, and (c) SH. In each figure, mean values are compared for three spatial heterogeneity situations as distinguished by ISCCP: homogeneous single-layer cloud (■), heterogeneous single-layer cloud (○), and multilayer clouds (△).

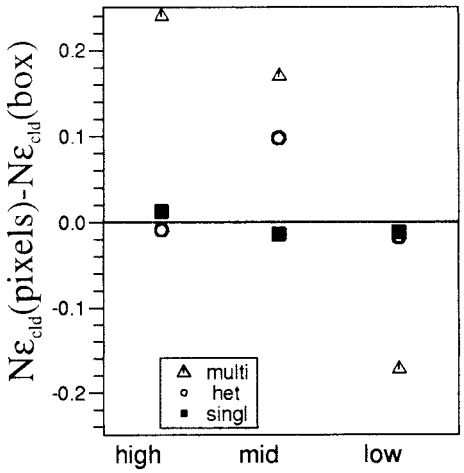

FIG. 4. Mean values of the difference between $N\varepsilon_{cld}$ determined by 3I for each individual cloudy HIRS pixel and by 3I for the average of cloudy HIRS pixels within a 1° × 1° grid box for high-, mid-, and low-level clouds as identified by 3I. Mean values are compared for three spatial heterogeneity situations: homogeneous single-layer cloud (■, same 3I pixel cloud type over 1° grid), heterogeneous single- layer cloud (○, same 3I pixel cloud height but heterogeneous $N\varepsilon_{cld}$), and multilayer clouds (△, different 3I pixel cloud heights and $N\varepsilon_{cld}$). Data are analyzed over tropical ocean for 3 days in July 1987.

the averaged cloudy radiances per box, whereas it is the contrary for low clouds. This means that the εN difference between ISCCP and 3I for multilayer clouds can be mostly explained by the fact that a lower $N\varepsilon_{cld}$ is obtained for a mixture of cirrus clouds with underlying stratus by first averaging the radiances and then using the 3I weighted-χ^2 method than by applying the 3I weighted-χ^2 method to every pixel and then averaging the pixel values. The ISCCP radiance sampling seems to increase the εN value in the case of horizontal cloud heterogeneities and multilayer clouds determined as low clouds by 3I.

A second investigation uses the VIS channel of the HIRS instrument. Since the HIRS VIS reflectances have been averaged, like the other HIRS radiances used for cloud parameter retrieval, over all cloudy HIRS pixels within a 1° × 1° region, this additional approach should clarify effects coming from averaging/sampling between 3I and ISCCP. The same correlations between cloudy VIS reflectance and cloud optical thickness τ as in ISCCP (Fig. A1) have been used to transform the cloudy HIRS VIS reflectances into cloud optical thicknesses τ. Corrections due to viewing geometry have been neglected. Then, $N\varepsilon_{cld}$ is calculated by applying Eq. (4). The mean differences between εN obtained from the cloudy VIS reflectance and εN determined from the 3I weighted-χ^2 method (over the box) are shown in Figs. 5a–c, separately for high-, mid-, and low-level clouds and for the three cloud heterogeneity conditions determined by ISCCP as described above. The best agreement is for high single-layer clouds and for multilayer clouds determined as low clouds by 3I. All these cloud categories have a large cloud cover. In all other cases the εN from the VIS is larger than from the IR, again

TABLE 1. Average frequency of appearance of 3I-pixel cloud types within 3I boxes, for each of the seven 3I-box cloud types: Cb, cumulonimbus; Ci, cirrus; thi Ci, thin cirrus; As, altostratus; Ac, altocumulus; St, stratus; and Cu, cumulus. Data are analyzed over tropical ocean for 3 days in July 1987.

3I box/3I pixel	Cb	Ci	th Ci	As	Ac	St	Cu
Cb	84%	15%	0%	1%	0%	0%	0%
Ci	17%	52%	20%	6%	1%	4%	0%
Thin Ci	0%	9%	64%	2%	3%	21%	1%
As	1%	4%	4%	66%	7%	17%	1%
Ac	0%	1%	15%	11%	26%	38%	8%
St	0%	0%	7%	2%	3%	75%	12%
Cu	0%	0%	1%	0%	2%	24%	64%

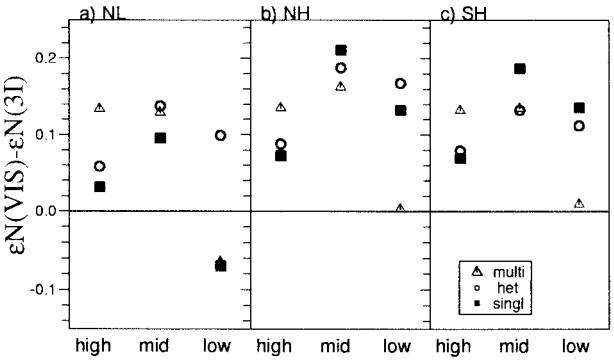

FIG. 5. Monthly mean values of the difference between εN determined by 3I from averaged cloudy VIS radiances and from averaged cloudy IR radiances at 1° spatial resolution for high-, mid-, and low-level clouds as identified by 3I. Three geographical regions, under sun illumination (in summer), are considered: (a) NL, (b) NH, and (c) SH. In each figure, mean values are compared for three spatial heterogeneity situations as distinguished by ISCCP: homogeneous single-layer cloud (■), heterogeneous single-layer cloud (○), and multilayer clouds (△).

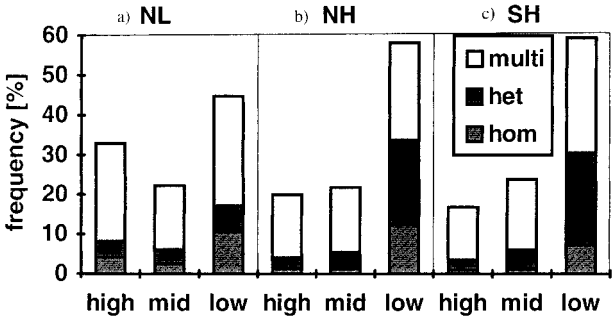

FIG. 6. Monthly mean frequencies of 3I high-, mid-, and low-level clouds and the distribution of homogeneous single-layer cloud, heterogeneous single-layer cloud, and multilayer clouds within each of the cloud-height categories for three geographical regions: (a) NL, (b) NH, and (c) SH.

demonstrating the differing effects of averaging reflectivities and emissivities. The small difference between homogeneous single-layer clouds and horizontally heterogeneous single-layer clouds indicates again that the difference between ISCCP and 3I comes from the difference between sampling and averaging. A slightly larger difference (5%) for high multilayer clouds indicates lower clouds seen by the VIS underneath cirrus.

The frequency of occurrence of these different cloud types under the three different heterogeneity conditions mentioned above is given in Figs. 6a–c for the three studied regions. As one can deduce from these figures, at a spatial resolution of $1° \times 1°$, most of the cloud scenes are heterogeneous. More precise studies on single-layer cirrus clouds can be done [e.g., retrieval of cirrus ice crystal sizes; see Stubenrauch et al. (1999b)], by eliminating cirrus clouds that have a higher effective emissivity computed from the visible information than the one retrieved by the 3I weighted-χ^2 method. One also can use combined AVHRR and HIRS measurements to obtain information on both cloud layers as was shown by Baum et al. (1994) in a regional study over ocean at nighttime.

b. τ–ε correlations

In this section, we want to focus on the cloudy pixels within the 1° grid to see if one can explain the correlation between the mean cloud optical thickness, τ, retrieved by ISCCP, and the mean IR cloud emissivity (or effective cloud amount over cloudy HIRS pixels), $N\varepsilon_{\text{cld}}$, retrieved by 3I, separately for high-, mid-, and low-level cloud fields. To avoid differences in cloud identification (discussed in Parts I and II) we consider only clouds that have been classified by both 3I and ISCCP as the same cloud height type (high, mid-, or low level). Over the North Atlantic, the match between ISCCP and 3I cloud height type is about 70%. At first, homogeneous and heterogeneous cloud situations are mixed.

Figure 7a shows $N\varepsilon_{\text{cld}}$ as a function of cloud optical thickness τ for the North Atlantic region. Then, τ is radiatively averaged [method 2 in the appendix]; $N\varepsilon_{\text{cld}}$ is averaged over about 25–2000 points, which fall into each of the 10 τ intervals. The observational relationship is less steep than the expected exponential behavior [shown for water and for ice clouds, see Eq. (4)], especially for low- and midlevel clouds.

In the appendix (Fig. A2) we show how we deduced that the IR cloud emissivity calculated from the radiatively averaged τ [Eq. (A3)] can reach values up to 10% larger than the mean pixel IR cloud emissivities [Eq. (A2)]. Therefore it would be better to recalculate τ from the averaged cloud emissivity [Eq. (A2)]. Indeed, Fig. 7b shows a slightly better relationship between

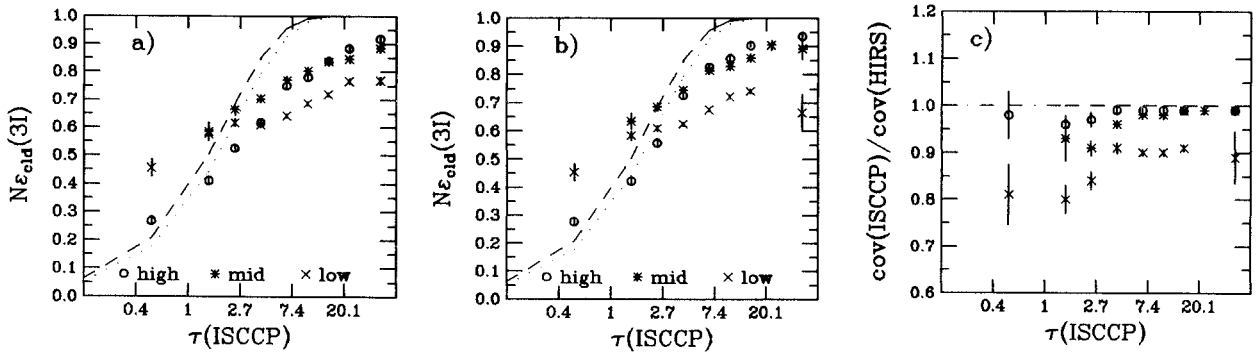

FIG. 7. (a) Average 3I effective IR cloud emissivity $N\varepsilon_{\text{cld}}$ as a function of ISCCP VIS cloud optical thickness τ (radiatively averaged, method 2 in the appendix), separately for high-, mid-, and low-level clouds over the Northern Hemisphere midlatitude ocean in Jul 1987 (sun illuminated). Error bars indicate the statistical error on $N\varepsilon_{\text{cld}}$. The scale of τ is logarithmic. All cloud covers and all types of heterogeneity situations are included. For comparison, theoretical curves calculated with Eq. (4) for water (·····) and ice (– – –) clouds are shown. (b) Average 3I $N\varepsilon_{\text{cld}}$ as a function of ISCCP τ (recalculated from averaged emissivity, method 1 in the appendix), separately for high-, mid-, and low-level clouds over Northern Hemisphere midlatitude ocean in Jul 1987 (sun illuminated). Error bars indicate the statistical error on $N\varepsilon_{\text{cld}}$. The scale of τ is logarithmic. All cloud covers and all types of heterogeneity situations are included. For comparison, theoretical curves calculated with Eq. (4) for water (– – –) and ice (·····) clouds are shown. (c) Average ratio of ISCCP and HIRS cloud cover fractions (at 1° spatial resolution) as a function of ISCCP τ (recalculated from averaged emissivity, method 1 in the appendix), separately for high-, mid-, and low-level clouds. Error bars indicate the statistical error on the ratio. The scale of τ is logarithmic.

$N\varepsilon_{cld}$ and τ, as calculated by method 1 of the appendix, for high clouds compared to the expected behavior. Subgrid-scale cloud heterogeneities still seem to play an important role in determining this relationship between the two datasets (as we will show) because the pixel size for HIRS is about four times larger than the pixels used by ISCCP. That the effect is stronger for low-level clouds is consistent with the correlated variations of optical thickness and cloud cover, as well as the strength of the instrument resolution effect on cloud cover, that have been observed by others (Sèze and Rossow 1991; Wielicki and Parker 1992; Rossow et al. 1993): in general, low-level clouds appear to be broken and more variable at smaller scales than upper-level clouds. Figure 7c illustrates this conclusion by showing that the average ratio of the ISCCP and HIRS cloud cover is about one for high-level clouds in all τ ranges, whereas it is progressively smaller than one for midlevel and low-level clouds with lower τ, meaning that the cloud cover determined by the higher-resolution ISCCP becomes progressively smaller than the matched results from the lower-resolution HIRS as cloud height and optical thickness decrease. Note however, that the magnitude of the cloud cover difference is only about 10%–20% (relative); thus, the less steep relationship between IR emissivity and visible optical thickness is produced, in general, by subpixel cloud variations, of which broken cover is just one extreme. Given the spectrum of cloud sizes and scales of their variability, these results should be general whenever two datasets with very different spatial resolutions are compared.

Another reason for disagreement with the theoretical curves is cloud heterogeneity. By eliminating all heterogeneous cloud scenes (heterogeneous in optical thickness as well as multilayer clouds as described in section 3a) and by considering only overcast cloud scenes, however, only three points are left for high clouds in Fig. 8. These are indeed slightly closer to the theoretical curves. The remaining points for midlevel and low-level clouds have a much smaller $N\varepsilon_{cld}$ than they should have for their optical thickness. This may be explained by cases where the 3I and ISCCP cloud covers agree, but there are still subpixel heterogeneities at scales smaller than 5 km, which can be frequent for low-level clouds.

The possible effect of multilayer clouds and subpixel heterogeneities can also be studied using the Goddard Institute for Space Studies (GISS) global circulation model (GCM), in which a cloud overlapping scheme has been implemented to obtain a more realistic behavior of radiative cloud properties (Stubenrauch et al. 1997). A prognostic cloud water parametrization scheme (Del Genio et al. 1996) provides stratiform and convective cloud covers and interactive optical thicknesses, τ_i, in nine atmospheric layers, i, at a spatial resolution of 4° latitude × 5° longitude. The subgrid cloud overlap scheme forms cloud ''blocks'' from adjacent cloud layers using maximum overlap. Different

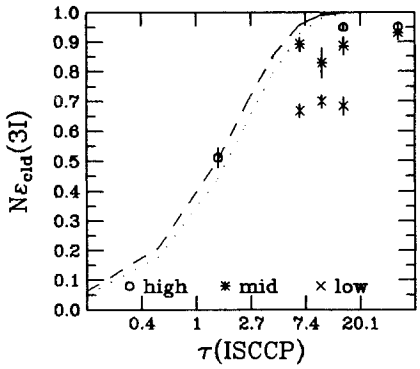

FIG. 8. Average 3I $N\varepsilon_{cld}$ as a function of ISCCP τ (recalculated from averaged emissivity, method 1 in the appendix), separately for overcast and homogeneous single-layer high-, mid-, and low-level clouds (at 1° spatial resolution) over Northern Hemisphere midlatitude ocean in Jul 1987 (sun illuminated). Error bars indicate the statistical error on $N\varepsilon_{cld}$. The scale of τ is logarithmic. Compared to Fig. 6b, the averages are formed from far fewer data points, because only overcast (100% cloud cover) and homogeneous cloud types are taken into account. For comparison, theoretical curves calculated with Eq. (4) for water (– – –) and ice (·····) clouds are shown.

cloud blocks are separated by an atmospheric layer of clear sky and are assumed to overlap randomly inside the grid box.

For a simulation of smaller grids (like the observational data at 1° spatial resolution), we allow an overlap of up to two cloud blocks. As illustrated in Fig. 9, the situation of two overlapping cloud blocks leads to three completely cloud-covered columns: 1) cloud block 1 with τ_1 only, 2) cloud block 1 and cloud block 2 overlapping with $\tau_{12} = \tau_1 + \tau_2$, and 3) cloud block 2 with τ_2 only. We calculate the average τ over the whole grid by the following procedure: we first transform the optical thickness of each column into the IR cloud emissivity by applying Eq. (4), then we average the IR cloud emissivity over the grid as the column fraction-weighted sum of the individual column cloud emissivities, and finally the average ε is retransformed into average τ over the whole grid using again Eq. (4).

The effective IR cloud emissivity, ε, as calculated in the 3I algorithm, is calculated as the ratio of radiance differences, at 11 μm:

$$\varepsilon = \frac{I_m(11\ \mu\text{m}) - I_{clr}(11\ \mu\text{m})}{I_{cld}(11\ \mu\text{m}) - I_{clr}(11\ \mu\text{m})}, \qquad (5)$$

where I_m is the averaged outgoing IR radiance over the cloud blocks inside the GCM grid box, correctly computed for each completely cloud-covered column, containing different overlapping cloud layers. In the second scheme of Fig. 9, for example, I_m is calculated separately for the three different, completely cloud-covered, columns and then summed up, each I_m weighted by the calculated fraction of the corresponding column. Here,

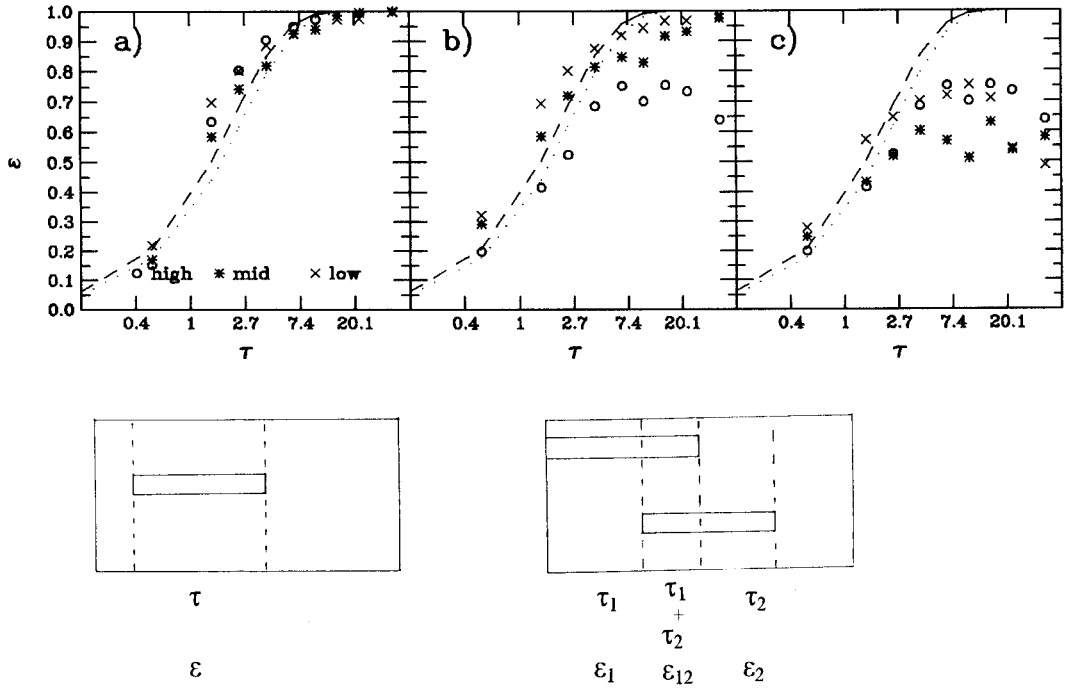

FIG. 9. Average IR cloud emissivity ε as a function of cloud optical thickness τ, separately for high-, mid-, and low-level clouds, as simulated by the GISS GCM using an implemented cloud overlap scheme: (a) for cases with one cloud block consisting of a single cloud layer; (b) for cases with up to two overlapping cloud blocks, consisting each of a single cloud layer, simulating multilayer clouds; and (c) like (b) but partly covered pixels are simulated for midlevel and low-level clouds. For comparison, theoretical curves calculated with Eq. (4) for water (– – –) and ice (·····) clouds are shown. A scheme of each cloud block situation (homogeneous single-layer cloud and multilayer clouds) is also indicated.

I_{clr} is the outgoing IR radiance for clear sky conditions and I_{cld} is the outgoing IR radiance for an overcast and opaque cloud with the gridbox-averaged cloud-top pressure as seen from satellites. For more details see Stubenrauch et al. (1997).

Indeed, in the case of one cloud block, consisting of one single layer, covering the whole GCM grid box, one observes the expected exponential relationship between ε and τ (Fig. 9a, small discrepancies from the theoretical behavior can be explained by the rough vertical resolution of the GCM). By allowing overlapping clouds (consisting of one cloud layer) to represent the case of multilayered clouds in the data (Fig. 9b), the relationship changes for high-level clouds, but not for low-level clouds. Note, however, that the GCM computes τ and ε over completely cloud-covered columns, whereas satellite observations occasionally retrieve these values over partly cloudy pixels, especially in the case of small-sized low-level clouds. The relationship gets closer to the experimentally observed correlations in Fig. 9c, when partly cloudy pixels are simulated by multiplying the cloud emissivity by cloud cover for low-level and midlevel clouds. The stronger change for high-level clouds in the model than in the data can be explained by the fact that the model distinguishes only nine atmospheric layers and therefore I_{cld} is calculated with low vertical resolution.

4. Cloud radiative effects

In the following we compare the outgoing LW and reflected SW radiative fluxes coming from scenes containing the different cloud types identified by 3I and by ISCCP. Since the radiative fluxes at the top of the atmosphere (TOA) are taken from ERBE, for both 3I and ISCCP clouds, we do not have to worry about disagreements in the radiation budget, and the differences shown indicate different assignments of fluxes to different cloud-type categories. This analysis will give us radiative flux uncertainties due to cloud-type classification and is therefore important for climate studies concerning detailed comparisons between cloud radiative effects of GCMs and those observed by satellite.

After examining the general relation between regional ERBE outgoing LW fluxes (OLR) and cloud and atmospheric properties obtained from 3I and ISCCP in section 4a, we compare in section 4b the radiative effects of different cloud types identified by 3I and by ISCCP, respectively. In both cases, these cloud types are distinguished by cloud-top pressure and effective cloud

amount, where 3I directly determines the effective cloud IR emissivity and ISCCP computes the cloud optical thickness, which can then be transformed into effective cloud IR emissivity. The average LW and SW radiative behaviors of these 3I and ISCCP cloud types are summarized in section 4c. Then we look in more detail at the effects of cloud spatial heterogeneity on the outgoing atmospheric radiative fluxes in section 4d.

a. Relationship between regional OLR and atmospheric properties

Figure 10 shows the monthly mean ERBE outgoing LW flux, 3I and ISCCP cloud-top temperatures, 3I and ISCCP effective cloud amount and cloud cover, as well as the 3I and ISCCP surface temperatures for selected geographical regions (cf. Fig. 11 in Part I) for summer and for winter. Note that in the winter hemisphere (not illuminated by the sun at 0730 LT) ISCCP effective cloud amount is just the cloud cover and, therefore, larger than the 3I effective cloud amount. Also during night, the ISCCP cloud-top temperature is not corrected for optical thickness effects. The much larger LW flux difference between summer and winter over land than over ocean is associated with a much larger surface temperature difference, but air temperatures also change correspondingly. Over the Southern Hemisphere, which is predominantly ocean with little land, the fluxes are nearly constant with season: the effect of colder clouds and lower effective cloud amounts during winter cancel each other. Generally, during daytime (summer), the 3I and ISCCP monthly mean regional cloud-top temperatures and effective cloud amounts are similar. The 3I cloud cover is about 10% larger than the ISCCP cloud cover due to the larger pixel size and better thin cirrus detection sensitivity of the former [see also section 3b(2) in Part I]. Over Northern Hemisphere land during daytime, however, both cloud cover fractions are the same, due to an IR threshold change over land in the ISCCP reprocessing. The ISCCP surface temperature (Rossow et al. 1996) is obtained only for clear sky, whereas the 3I algorithms undertake a cloud clearing of radiances from partly cloudy scenes. Thus, in cases where the cloud cover difference is larger, the ISCCP clear sky surface temperature is slightly smaller than the 3I surface temperature, indicating a possible cloud contamination of the ISCCP values but also consistent with the clear sky bias effect discussed by Rossow et al. (1993).

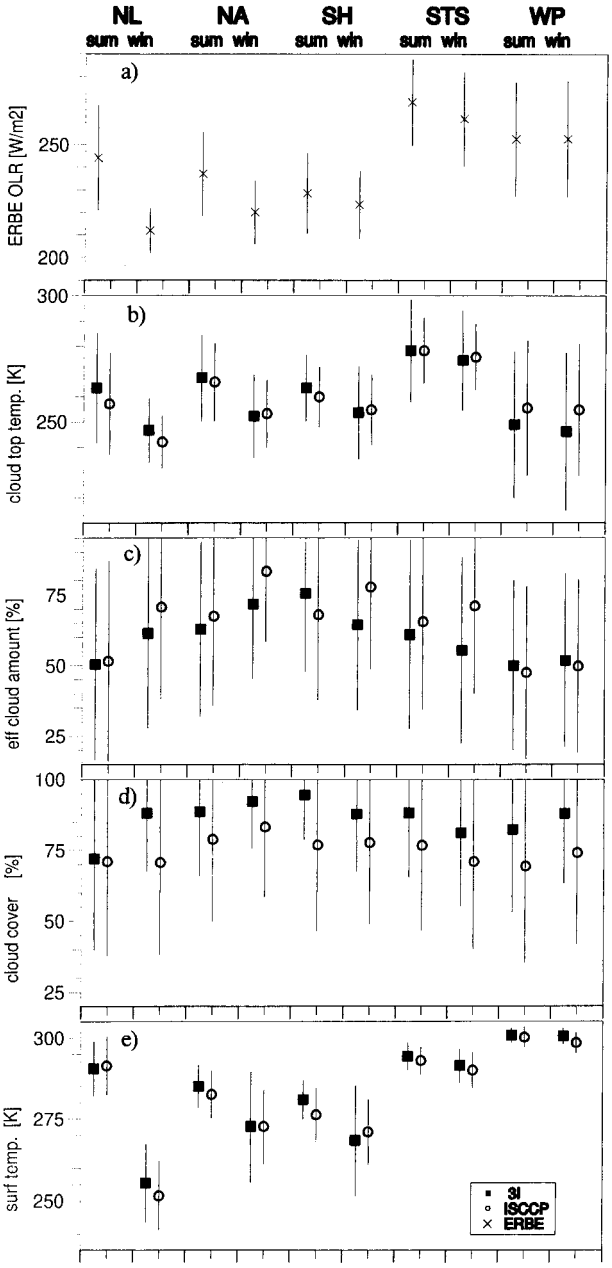

FIG. 10. Monthly mean regional averages and standard deviations of (a) ERBE outgoing LW flux, (b) 3I and ISCCP cloud-top temperature, (c) 3I and ISCCP effective cloud amount, (d) 3I and ISCCP cloud cover fraction, and (e) 3I and ISCCP surface temperature in summer and in winter, for Northern Hemisphere midlatitude (40°–70°N) land, North Atlantic (40°–70°N), Southern Hemisphere midlatitude ocean (40°–70°S), marine stratocumulus regions off the Southern Hemisphere western continental coasts (Namibia, 10°–30°S; Australia, 10°–40°S; and South America 15°–50°S), and the tropical warm pool (10°S–10°N, 70°E–160°W).

b. Cloud-type-dependent radiative effects

The change in the outgoing LW fluxes induced by the presence of clouds can be estimated[1] by the difference between monthly mean clear sky outgoing LW flux and monthly mean cloudy outgoing LW flux over the same region [Eqs. (6) and (7)]. Respectively, the change in reflected SW fluxes induced by the presence of clouds

[1] This procedure produces only an estimate because it does not remove systematic changes of the atmosphere and surface that might be correlated with cloudiness changes.

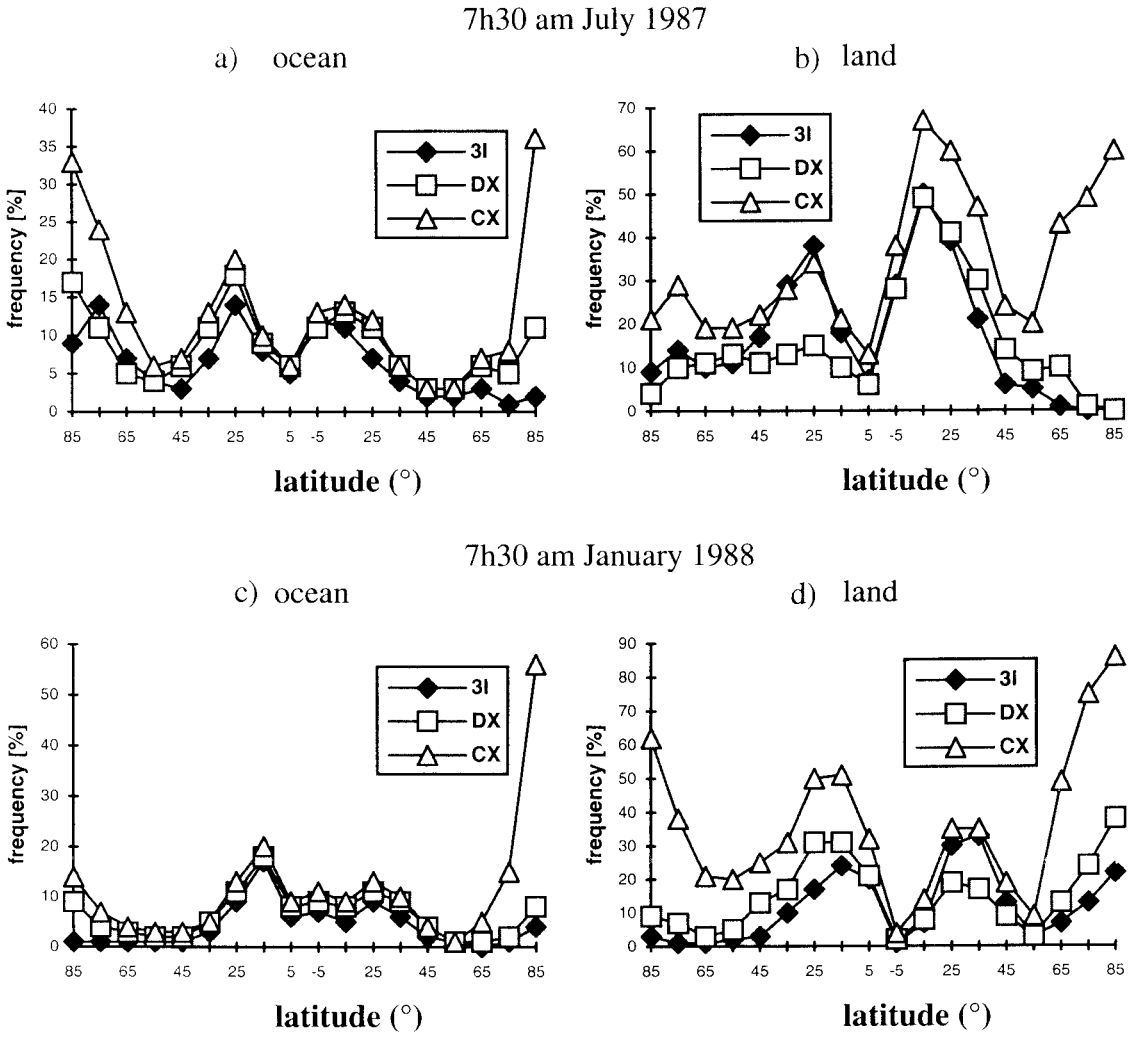

FIG. 11. Zonal monthly mean clear sky frequencies (at a spatial resolution of 1° × 1°) at 0730 LT Jul 1987 (a) and (b) and in January 1988 (c) and (d), over ocean (a) and (c) and over land (b) and (d), as identified by current ISCCP (CX), reprocessed ISCCP (DX), and by 3I.

can be estimated by the difference between the monthly mean clear sky reflected SW flux divided by the cosine of the sun zenith angle (corresponding to the albedo times the incoming solar radiation) and the monthly mean cloudy reflected SW flux divided by the cosine of the sun zenith angle over the same region [Eqs. (8) and (9)]. Without distinguishing different cloud types, this difference, henceforth called cloud-induced radiative flux change (CRFC), is larger than the so-called cloud radiative forcing (e.g., Ramanathan et al. 1989; Stephens and Greenwald 1991), which is the difference between clear sky and total (mixed clear and cloudy) fluxes. Since the general effect of clouds is to reduce the outgoing LW flux at TOA, which is equivalent to a warming of the earth, and increase the outgoing SW flux at TOA, which is equivalent to a cooling of the earth, we will refer to the cloud LW effect as a ''cloud warming'' and to the cloud SW effect as a ''cloud cooling.'' The analysis of *NOAA-10* observations alone provides estimates of cloud warming and cooling as well as of their net radiative effect at about 0730 LT. In order to reduce uncertainties in ERBE SW flux retrieval, only situations with the sun zenith angle $\theta_0 < 65°$ were used for the analysis of cloud SW and net radiative effects:

$$\overline{\mathrm{CRFC}}^{\,3\mathrm{I}}_{\mathrm{LW}}(1° \times 1°) = F^{\mathrm{ERBE}}_{\mathrm{LW}}(1° \times 1° \text{ 3I clear sky}) - F^{\mathrm{ERBE}}_{\mathrm{LW}}(1° \times 1° \text{ 3I cloudy}), \quad (6)$$

$$\overline{\mathrm{CRFC}}^{\,\mathrm{ISCCP}}_{\mathrm{LW}}(1° \times 1°) = F^{\mathrm{ERBE}}_{\mathrm{LW}}(1° \times 1° \text{ ISCCP clear sky}) - F^{\mathrm{ERBE}}_{\mathrm{LW}}(1° \times 1° \text{ ISCCP cloudy}), \quad (7)$$

$$\overline{\mathrm{CRFC}}^{\,3\mathrm{I}}_{\mathrm{SW}}(1^\circ \times 1^\circ) = F^{\mathrm{ERBE}}_{\mathrm{SW}}(1^\circ \times 1^\circ \text{ 3I clear sky})/\cos\theta_0 - F^{\mathrm{ERBE}}_{\mathrm{SW}}(1^\circ \times 1^\circ \text{ 3I cloudy})/\cos\theta_0, \quad (8)$$

$$\overline{\mathrm{CRFC}}^{\,\mathrm{ISCCP}}_{\mathrm{SW}}(1^\circ \times 1^\circ) = F^{\mathrm{ERBE}}_{\mathrm{SW}}(1^\circ \times 1^\circ \text{ ISCCP clear sky})/\cos\theta_0 - F^{\mathrm{ERBE}}_{\mathrm{SW}}(1^\circ \times 1^\circ \text{ ISCCP cloudy})/\cos\theta_0. \quad (9)$$

In our analysis, the ERBE fluxes (outgoing LW or reflected SW divided by the cosine of the sun zenith angle θ_0) determined per pixel have first been averaged over the $1^\circ \times 1^\circ$ regions. The monthly mean regional clear sky flux is then determined by collecting the 1° grid ERBE fluxes during the month, only when the whole 1° grid is clear according to 3I or to ISCCP, respectively. Zonally averaged clear sky frequencies are given in Figs. 11a–d for clear sky identification by 3I, DX, and CX. Differences in cloud detection are described in section 3b(2) of Part I. In general, the 3I and DX clear sky frequencies agree quite well (with the exception of desert in summer). Improved ISCCP cloud detection by using the 3.7-μm channel of AVHRR at higher latitudes ($>50^\circ$) leads to a better agreement with 3I in the polar regions. The monthly mean regional cloudy flux is obtained by collecting the 1° grid ERBE fluxes during the month over the rest of the $1^\circ \times 1^\circ$ regions (containing clouds detected by 3I or by ISCCP, respectively). Equations (6) to (9) can be refined by considering the warming and cooling effect of different cloud types (hereafter ''cldtyp''):

$$\mathrm{CRFC}^{\mathrm{3I\,cldtyp}}_{\mathrm{LW}}(1^\circ \times 1^\circ) = F^{\mathrm{ERBE}}_{\mathrm{LW}}(1^\circ \times 1^\circ \text{ 3I clear sky}) - F^{\mathrm{ERBE}}_{\mathrm{LW}}(1^\circ \times 1^\circ \text{ 3I cldtyp}), \quad (10)$$

$$\mathrm{CRFC}^{\mathrm{ISCCP\,cldtyp}}_{\mathrm{LW}}(1^\circ \times 1^\circ) = F^{\mathrm{ERBE}}_{\mathrm{LW}}(1^\circ \times 1^\circ \text{ ISCCP clear sky}) - F^{\mathrm{ERBE}}_{\mathrm{LW}}(1^\circ \times 1^\circ \text{ ISCCP cldtyp}), \quad (11)$$

$$\mathrm{CRFC}^{\mathrm{3I\,cldtyp}}_{\mathrm{SW}}(1^\circ \times 1^\circ) = F^{\mathrm{ERBE}}_{\mathrm{SW}}(1^\circ \times 1^\circ \text{ 3I clear sky})/\cos\theta_0 - F^{\mathrm{ERBE}}_{\mathrm{SW}}(1^\circ \times 1^\circ \text{ 3I cldtyp})/\cos\theta_0, \quad (12)$$

$$\mathrm{CRFC}^{\mathrm{ISCCP\,cldtyp}}_{\mathrm{SW}}(1^\circ \times 1^\circ) = F^{\mathrm{ERBE}}_{\mathrm{SW}}(1^\circ \times 1^\circ \text{ ISCCP clear sky})/\cos\theta_0 - F^{\mathrm{ERBE}}_{\mathrm{SW}}(1^\circ \times 1^\circ \text{ ISCCP cldtyp})/\cos\theta_0. \quad (13)$$

In Equations (10)–(13), the ERBE fluxes are averaged over $1^\circ \times 1^\circ$ regions containing the considered 3I cloud type or ISCCP cloud type, respectively. For the analysis of cloud-type-dependent radiative behavior, seven different cloud types are described below. The ISCCP cloud-type classification is matched to the 3I cloud-type classification as follows: we first transform the ISCCP optical thickness, τ, into an effective cloud emissivity, $N\varepsilon_{\mathrm{cld}}$, by using Eq. (4) and the averaging method 1 in the appendix. Multiplying with the ISCCP cloud cover fraction we otain an effective cloud amount, εN. Hence, using 3I or ISCCP data, respectively, high clouds ($p_{\mathrm{cld}} < 440$ hPa) can be divided into opaque ($N\varepsilon_{\mathrm{cld}} > 90\%$), cirrus ($90\% < N\varepsilon_{\mathrm{cld}} < 50\%$), and thin cirrus ($N\varepsilon_{\mathrm{cld}} < 50\%$); midlevel and low-level ($p_{\mathrm{cld}} > 680$ hPa) clouds can be separated into mostly cloudy ($\varepsilon N > 50\%$) and partly cloudy.

The cloud-type-dependent CRFCs in July are shown as a function of latitude in Figs. 12a–c for ocean and in Figs. 12d–f for land. Cloud types are identified by the first version of ISCCP (C series, Figs. 12a and 12d), by the reprocessed ISCCP (D series, Figs. 12b and 12e), and by 3I (Figs. 12c and 12f). Figure 13 shows the same for January. Note that in the winter hemisphere (Southern Hemisphere in July and Northern Hemisphere in January, not illuminated), ISCCP does not compute τ (because the VIS information is missing) and therefore no separation between optically thick and thin clouds is possible within one cloud-height category. In this case, ERBE fluxes are averaged over the whole cloud-height category and shown under the different opaque cloud-height categories in Figs. 12 and 13. However, 3I continues to give the full cloud-type information.

The global mean cloud warming effect is about 20 W m^{-2} at 0730 LT, the zonal mean cloud warming varies between <5 W m^{-2} for partly cloudy, low-level cloud fields and 150 W m^{-2} for overcast, high opaque clouds in the Tropics. The warming effect of cirrus reaches 80 W m^{-2}, followed by overcast midlevel clouds and thin cirrus with a maximum warming effect of 40 W m^{-2}.

A previous comparison between ISCCP C series, ISCCP D series, and 3I cloud parameters (section 3 of Part I) has already revealed an improvement due to the ISCCP reprocessing. This is also seen in the cloud classification and hence in the cloud-type-dependent ERBE flux averaging: During daytime (summer hemisphere), the reprocessed ISCCP (D series) cloud-type classification yields a larger cloud warming distinction between high opaque and cirrus clouds, in better agreement with results from the 3I cloud-type classification. Still, the 3I high opaque clouds have a cloud warming that is about 10 W m^{-2} larger than the ISCCP-identified high opaque clouds, especially in the Tropics (only for the illuminated summer hemisphere): this effect could result from the different interaction of the different wavelengths used in the two analyses with the very ''diffuse'' tops of most tropical clouds (Liao et al. 1995).

Since 3I provides full cloud identification during daytime (summer hemisphere) as well as during nighttime (winter hemisphere), we can compare the latitudinal cloud warming behavior over ocean (panels a–c) and over land (panels d–f) in July (Fig. 12) and January (Fig. 13). These figures not only show the expected seasonal shift of the strong cloud warming produced by

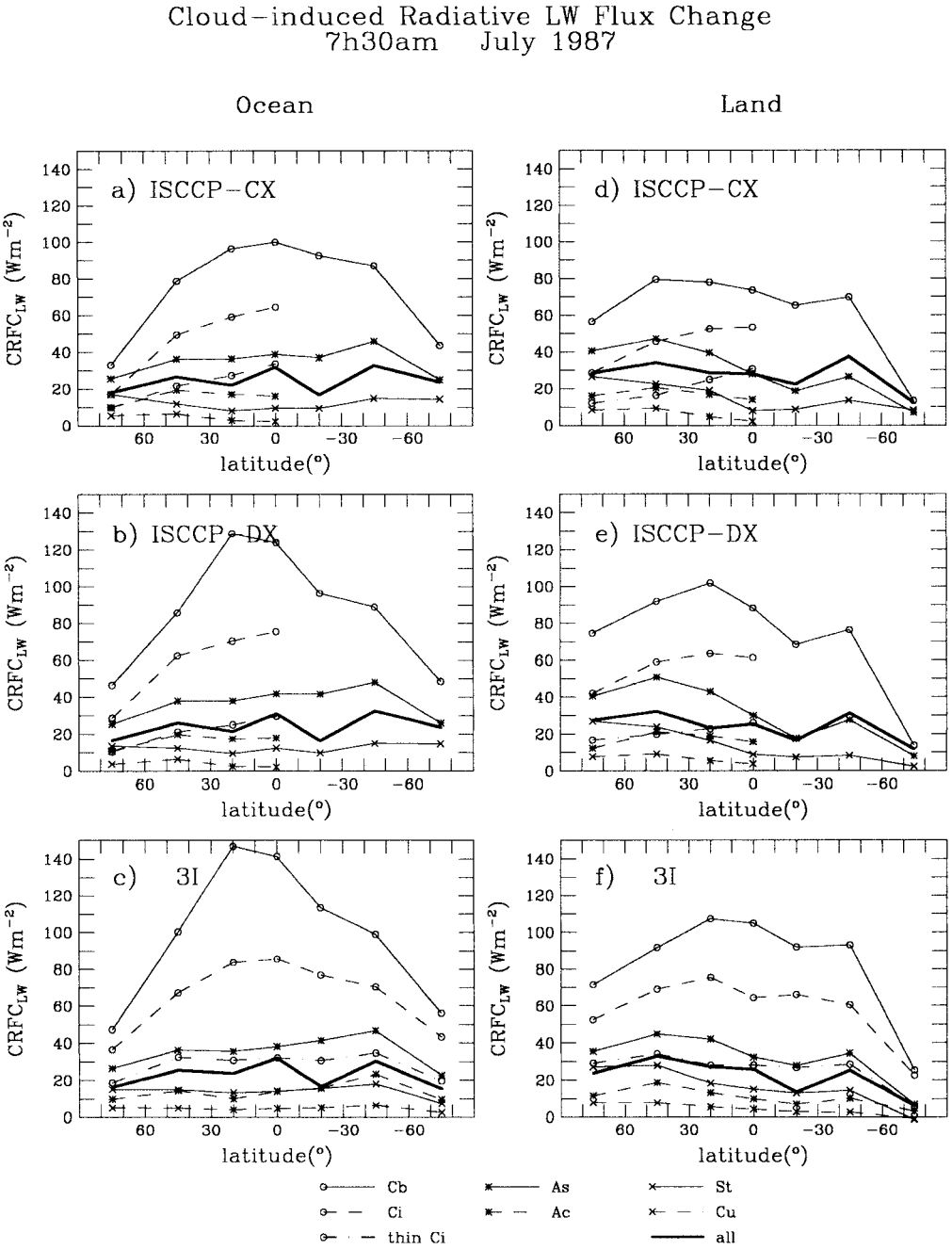

FIG. 12. Zonal cloud warming at 0730 LT Jul 1987 (sun illuminated in Northern Hemisphere and nighttime in Southern Hemisphere) for seven cloud types identified by (a), (d) current ISCCP, (b), (e) reprocessed ISCCP, and (c), (f) 3I, over ocean (a)–(c) and over land (d)–(e).

high opaque clouds in the intertropical convergence zone (ITCZ) from the summer to the winter hemisphere, but also that this feature is stronger over ocean in July and over land in January. For the same cloud type, cloud warming should be stronger in midlatitude summer than in winter because of larger surface temperatures, and hence larger clear sky outgoing LW fluxes (cf. Rossow and Zhang 1995). This effect can be seen over land, but over ocean the smaller surface temperature difference is compensated by larger atmospheric water vapor abundances. These cloud-type-dependent radiative effects can be compared to global circulation models (Stubenrauch et al. 1997) to gain a better understanding of parametrizations of different cloud types.

Whereas cloud warming depends on cloud height, optical thickness and cover, as well as on clear sky

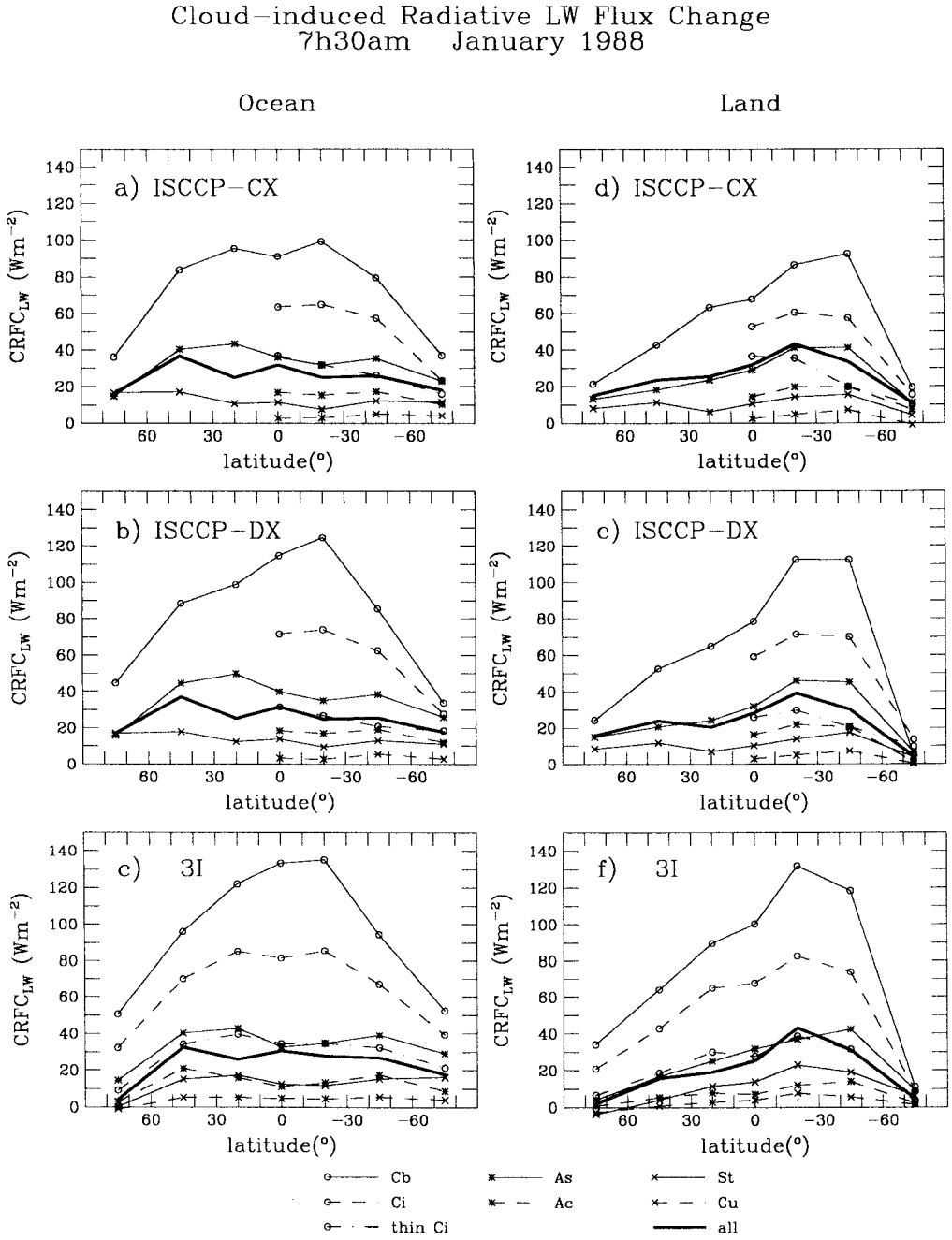

FIG. 13. Zonal cloud warming at 0730 LT Jan 1988 (sun illuminated in Southern Hemisphere and nighttime in Northern Hemisphere) for seven cloud types identified by (a), (d) current ISCCP, (b), (e) reprocessed ISCCP, and (c), (f) 3I, over ocean (a)–(c) and over land (d)–(e).

surface temperature and atmospheric water vapor abundance and vertical distribution, cloud cooling mostly depends on solar inclination (latitude), cloud optical thickness and cover, and surface albedo (see also, e.g., the regional studies of Ackerman et al. 1992; Rossow and Zhang 1995). At 0730 LT, cloud cooling reaches 300 W m^{-2} for high opaque clouds over the ITCZ. Cirrus have the same cooling effect as overcast midlevel clouds (maximum 200 W m^{-2}) and thin cirrus have the same effect as partly cloudy midlevel clouds (maximum 100 W m^{-2}; not shown, but can be inferred from the net CRFC and LW CRFC in Figs. 12–15). In contrast the warming effects of cirrus and of thin cirrus are stronger than those of overcast midlevel and of partly cloudy midlevel clouds, respectively (Figs. 12 and 13). Figures 14 (July) and 15 (January) show the zonal behavior of

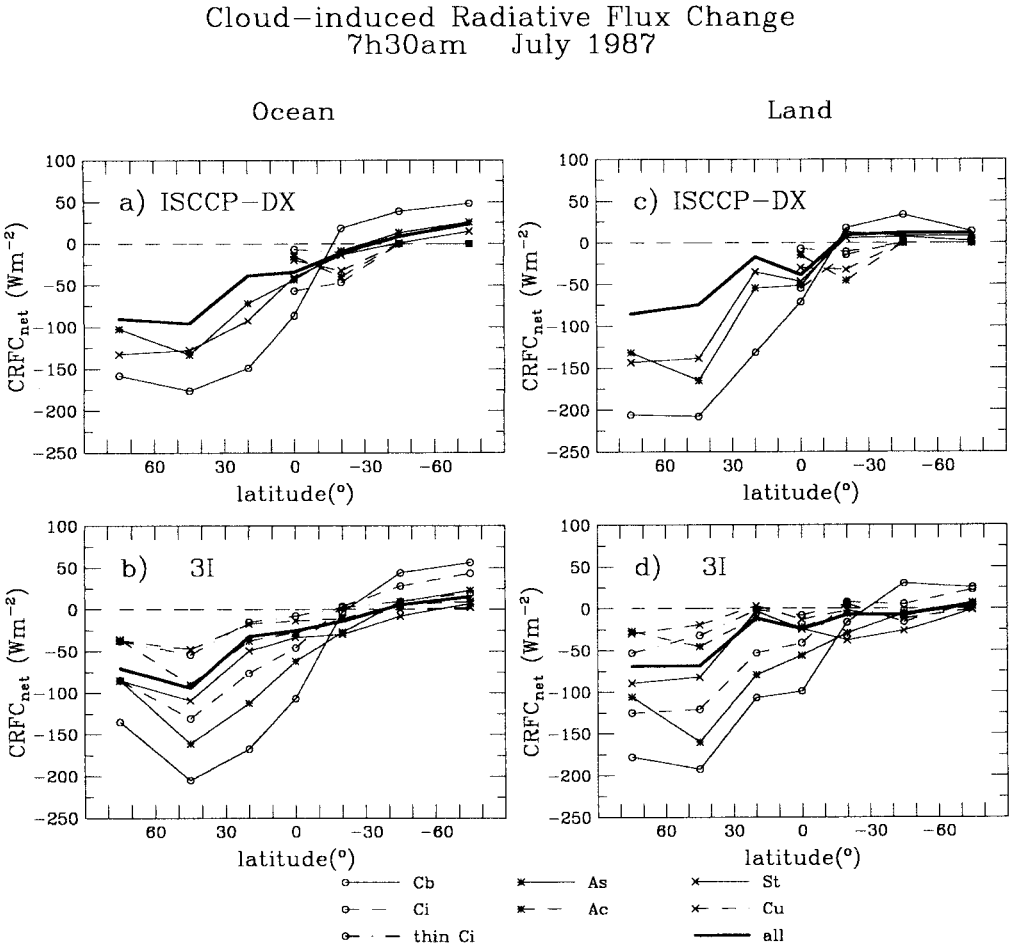

FIG. 14. Zonal cloud-induced net radiative effect at 0730 LT in Jul 1987 (sun illuminated in Northern Hemisphere and nighttime in Southern Hemisphere) for seven cloud types identified by (a), (c) reprocessed ISCCP and (b), (d) 3I, over ocean (a), (b) and over land (c), (d). Average solar zenith angles for the Northern Hemisphere latitude bands are 56°, 53°, 58°, and 62°.

the net CRFC, which is the sum of LW and SW cloud-induced flux change, separately over ocean (panels a and b) and over land (panels c and d), using the cloud-type classification with ISCCP cloud parameters (panels a and c) and with 3I cloud parameters (panels b and d), respectively. The SW CRFC can be computed only under daytime conditions, during night it is zero. The net radiative effect of cirrus identified by ISCCP (daytime) is smaller than for cirrus identified by 3I. This can be explained by the fact that 3I identifies both isolated cirrus as well as cirrus overlying lower clouds, whereas ISCCP on the other hand identifies only isolated cirrus as cirrus (see sections 3a and 4d). During daytime, clouds have a net cooling effect, depending very much on the solar inclination and cloud height for overcast clouds. Thin cirrus have the smallest net effect together with partly cloudy low-level clouds, whereas their warming effect is three times larger than that of partly cloudy low-level clouds.

c. Correlations of OLR and FSW with cloud types

As a summary, we characterize these seven 3I and ISCCP cloud types (see section 4b) by their average LW and SW radiative behavior over five selected geographical regions (shown in Fig. 11 of Part I): (a) NL, (b) North Atlantic (NA), (c) SH, (d) Southern Hemisphere stratocumulus regions (STS), and (e) tropical Pacific warm pool (WP). Figures 16a–e show these cloud-type-dependent average ERBE OLRs and reflected SW fluxes divided by the cosine of the solar zenith angle, FSW, together with their standard deviations, to show the radiative variability for each cloud type. Large dots label ISCCP cloud types whereas small dots label 3I cloud types. Clear sky average values, according to ISCCP and to 3I, respectively, are also given for these five geographical regions. In the midlatitudes, the span between clear sky and high opaque clouds is smaller than in the Tropics, where these clouds are much higher. In the stratocumulus regime (STS), the stratus clouds are

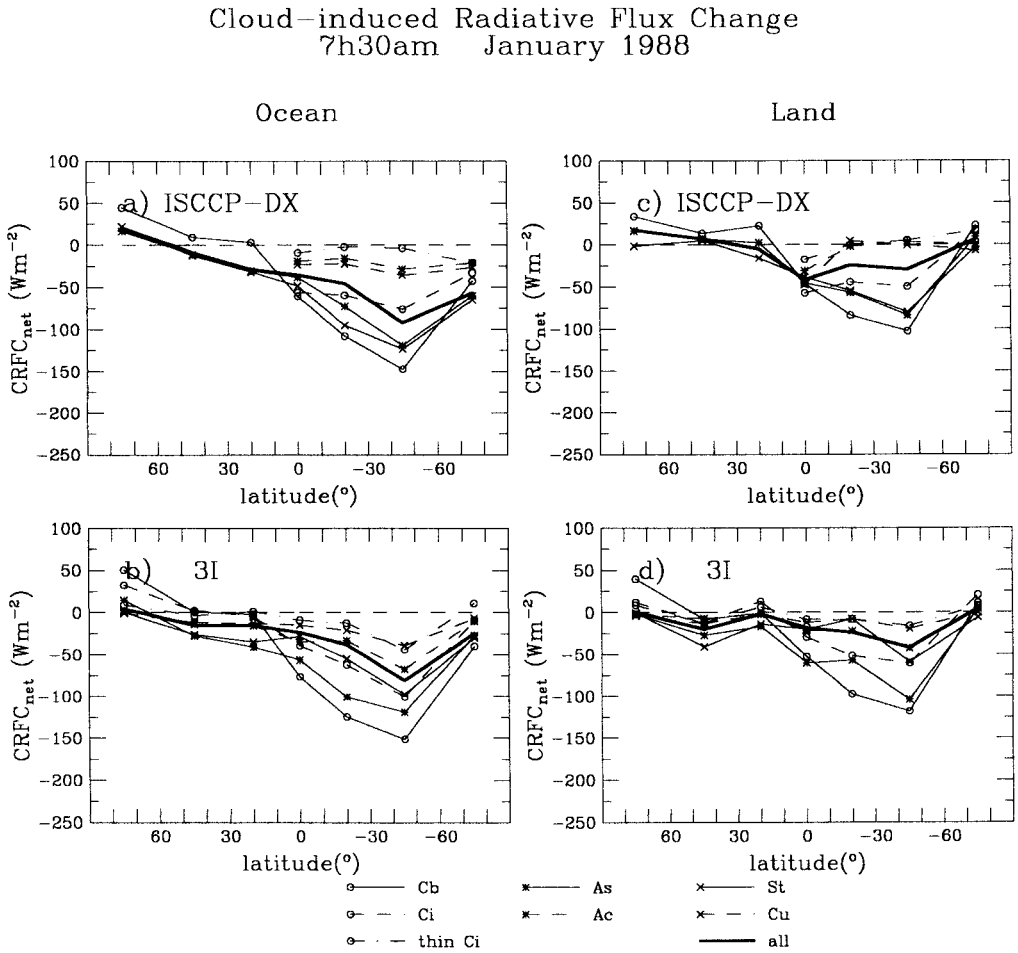

FIG. 15. Zonal cloud-induced net radiative effect at 0730 LT in Jan 1988 (sun illuminated in Southern Hemisphere and nighttime in Northern Hemisphere) for seven cloud types identified by (a), (c) reprocessed ISCCP and (b), (d) 3I over ocean (a), (b) and over land (c), (d). Average solar zenith angles for the Southern Hemisphere latitude bands are 63°, 61°, 62°, and 63°.

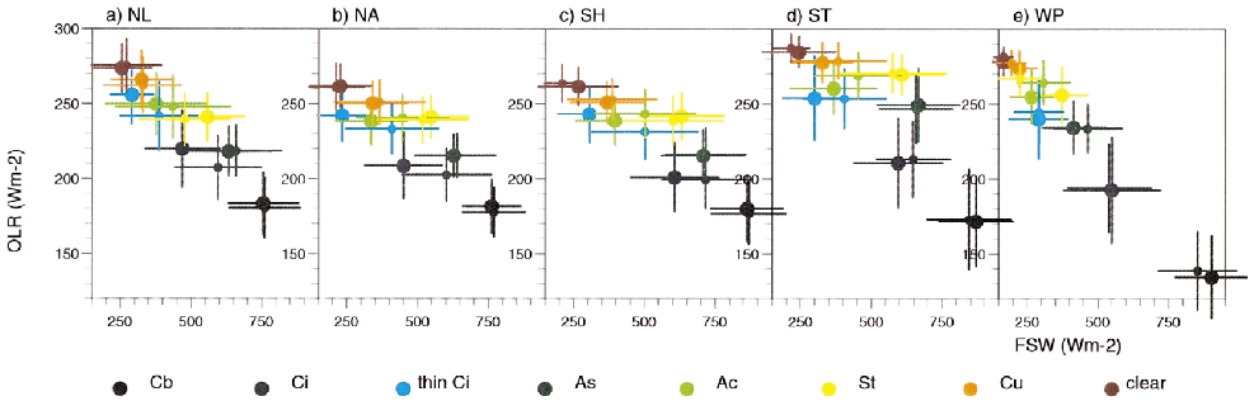

FIG. 16. Monthly mean regional averaged ERBE outgoing LW fluxes and reflected SW fluxes (divided by $\cos\theta_0$) of clear sky and seven cloud types identified by 3I (small dots) and ISCCP (large dots), for the geographical regions described in Fig. 9, in summer (sun illuminated): Cb, cumulonimbus; Ci, cirrus; thin Ci, thin cirrus; As, altostratus; Ac, altocumulus; St: stratus; and Cu, cumulus.

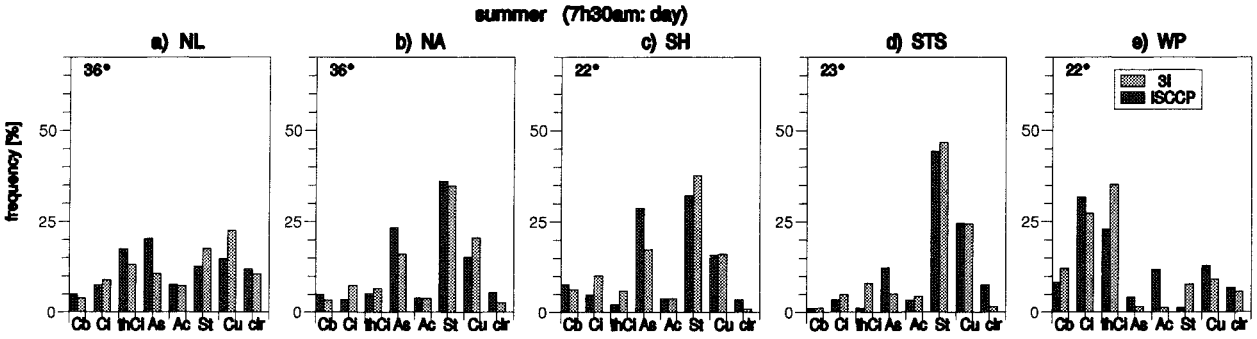

FIG. 17. Monthly mean clear sky and cloud-type frequencies as identified by 3I and ISCCP over the same geographical regions as in Fig. 14: (a) NL, (b) NA, (c) SH, (d) STS, and (e) WP. The sun elevation angle is also given for each region.

as reflective as, but warmer than, clouds in midlatitudes. For opaque clouds the associated radiative fluxes of 3I and ISCCP cloud types agree very well. Exceptions are stratus clouds in the WP and over NL. In these regions, the ISCCP cloud cover fraction is higher than the 3I cloud cover fraction, a sign for cloud sizes smaller than the HIRS pixel size, and therefore contributions from the surface may enter. The 3I cirrus and thin cirrus in midlatitudes are colder and more reflective, closer to ISCCP partly covered midlevel clouds than to ISCCP thin cirrus. The larger reflectance can be explained by multilayer clouds; the larger OLR of ISCCP thin cirrus can be explained by misidentification with thin low-level clouds. In general, one can observe that the high- and midlevel semitransparent ISCCP cloud types are darker than the corresponding cloud class identified by 3I. This effect will be further studied in section 4d. For complementary information, cloud-type frequencies for the same geographical regions are shown in Figs. 17a–e. Notice the very good agreement between ISCCP and 3I within 5%. Some of the 3I cirrus clouds (especially thin cirrus) are identified as midlevel clouds by ISCCP. Note that the differences shown here are not necessarily errors in the radiative effects of clouds determined by either 3I or ISCCP, but rather illustrate the effects of different cloud classifications coming from data differences (pixel sizes, averaging–sampling, and IR–VIS). Nevertheless, the subtle differences arise, in part, from the different effects of cloud heterogeneities on the two cloud analyses that change the relationship of VIS optical thickness and IR emissivity. These differences should be examined in more detail.

d. Correlations of effective cloud amounts with OLR and FSW

In the following we explore further the correlations between the radiative fluxes leaving the atmosphere, determined by ERBE, and the effective cloud amount εN, computed from averaged IR radiances by 3I and from sampled VIS radiances by ISCCP. We are especially interested in the change of behavior under different conditions of cloud heterogeneity. We discuss as an example results averaged over ocean in the latitude band from 30° to 60°N, but other latitude bands show similar behavior. The ERBE OLR is shown as a function of effective cloud amount as determined by ISCCP in Figs. 18a–c and as determined by 3I in Figs. 18d–f. For each of the three cloud-height categories, high (Figs. 18a and 18d), mid- (Figs. 18b and 18e), and low (Figs. 18c and 18f), as distinguished by ISCCP and by 3I, respectively, the behavior is studied separately for homogeneous single-layer clouds, for heterogeneous single-layer clouds, and for multilayer clouds (see section 3a). The differences between Figs. 18a and 18d, between Figs. 18b and 18e, and between Figs. 18c and 18f are also shown in Figs. 18g–i, respectively. Over the same $1° \times 1°$ region we have one ERBE OLR, one 3I effective cloud amount, and one ISCCP cloud amount. Therefore, these differences in the averaged ERBE LW fluxes can directly be interpreted as differences in sampling by 3I and ISCCP. In the same way, the ERBE-reflected SW fluxes, divided by the cosine of the solar zenith angle, FSW, are shown as a function of 3I and ISCCP effective cloud amounts, respectively, in Figs. 19a–f, and differences in Figs. 19g–i.

The average OLR over a region can be expressed as a function of effective cloud amount εN; the outgoing LW flux of the cloud considered as opaque, $F_{\text{cld}}^{\text{LW}}$; and the outgoing LW flux of clear sky, $F_{\text{clr}}^{\text{LW}}$:

$$\begin{aligned} \text{OLR} &= \varepsilon N(F_{\text{cld}}^{\text{LW}}) + (1 - \varepsilon N)F_{\text{clr}}^{\text{LW}} \\ &= \varepsilon N(F_{\text{cld}}^{\text{LW}} - F_{\text{clr}}^{\text{LW}}) + F_{\text{clr}}^{\text{LW}}. \end{aligned} \tag{14}$$

From Figs. 18a–f, one observes, as expected, a decrease of OLR with increasing εN, the slope increasing with cloud height. In the case of high clouds, the OLR decreases less for multilayer clouds than for homogeneous and heterogeneous single-layer clouds; again this is expected since the clouds beneath are warmer and hence their OLR is larger. The OLR exhibits a linear dependence on εN (computed by 3I from averaged IR radiances), with different slopes for single-layer and multilayer clouds, whereas the OLR's dependence on εN (computed by ISCCP from sampled VIS radiances) differs slightly from linear behavior in an opposite sense

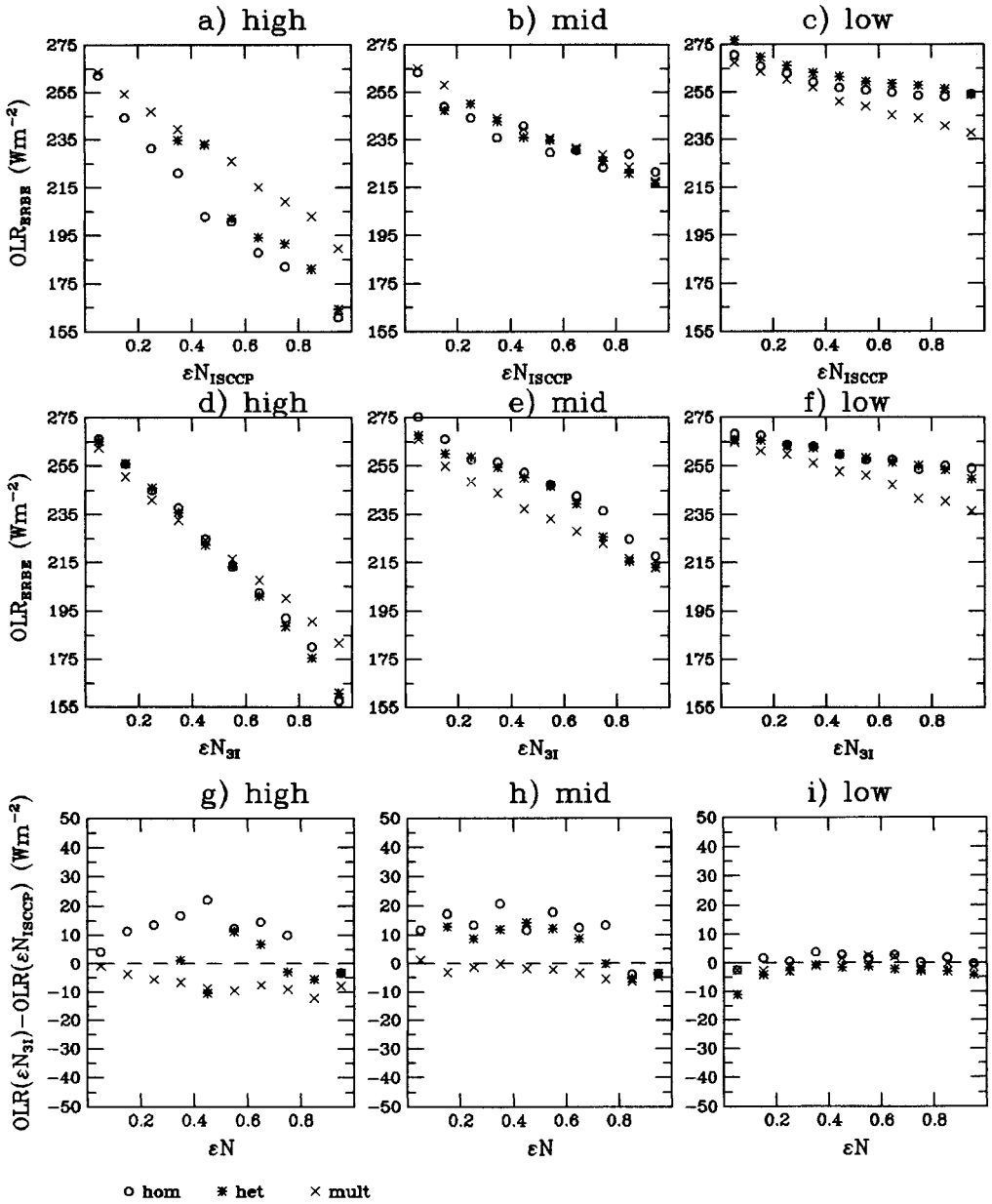

FIG. 18. (a)–(f) ERBE outgoing LW flux as a function of effective cloud amount, as determined by ISCCP (a)–(c) and by 3I (d)–(f), respectively, for high-, (a), (d), mid-, (b), (e), and low-level clouds (c), (f). For each cloud-height type, homogeneous (○) and heterogeneous one-layer clouds (*) as well as multilayer clouds (×) are considered. Observations are averaged over ocean between 30° and 60°N in Jul 1987. (g)–(i) Difference between ERBE outgoing LW fluxes sampled as a function of 3I and ISCCP effective cloud amount, for high- (g), mid- (h), and low-level clouds (i).

for single-layer and multilayer clouds. The nonlinear dependence comes, in part, from the different weighting given to emissivity values by VIS and IR measurements (see below).

Considering Figs. 18g–i, for transmissive, especially high- and midlevel, clouds ($\varepsilon N < 0.8$), we find that $\mathrm{OLR}_{\mathrm{ERBE}}(\varepsilon N_{3\mathrm{I}}) > \mathrm{OLR}_{\mathrm{ERBE}}(\varepsilon N_{\mathrm{ISCCP}})$, if $\varepsilon N_{3\mathrm{I}} = \varepsilon N_{\mathrm{ISCCP}}$ for homogeneous clouds, but $\mathrm{OLR}_{\mathrm{ERBE}}(\varepsilon N_{3\mathrm{I}}) < \mathrm{OLR}_{\mathrm{ERBE}}(\varepsilon N_{\mathrm{ISCCP}})$ if $\varepsilon N_{3\mathrm{I}} = \varepsilon N_{\mathrm{ISCCP}}$ for multilayer clouds. This means that for homogeneous, transmissive single-layer clouds, εN obtained from averaged IR radiances characterizes a warmer radiative field than the same εN obtained from sampled VIS radiances, or in other words, for the same LW radiative field, $\varepsilon N_{\mathrm{ISCCP}}$ is smaller than $\varepsilon N_{3\mathrm{I}}$. It is interesting to notice that a similar effect can be seen in Figs. 19a–c for the GCM (see section 3b) when we calculate εN from averaged IR radiances [Eq. (5)] on the one hand and from τ on the other, indicating that averaging VIS radiances or IR radiances does not lead to the same εN (see the mathe-

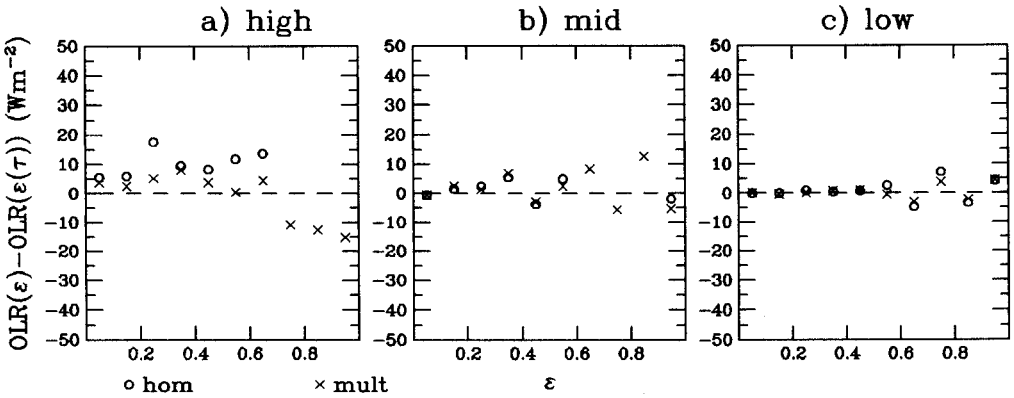

FIG. 19. (a)–(c) Difference between GCM-computed outgoing LW fluxes sampled as a function of VIS and IR effective cloud amount, for high- (a), mid- (b), and low-level clouds (c), separately for homogeneous (○), heterogeneous one-layer clouds (*), and multilayer clouds (×).

matical illustration in the appendix). Another part of the explanation comes from the different sampling within one cloud-height class: homogeneous, transmissive single-layer high- and midlevel clouds are found to have a larger average 3I cloud-top pressure than ISCCP cloud-top pressure (not shown).

In the case of multilayer clouds the same radiative field corresponds to a smaller εN_{3I} than εN_{ISCCP}. This case can be understood by the fact that ISCCP determines a small εN only for isolated cirrus layers, whereas 3I determines a small εN for cirrus overlying lower clouds as well as for isolated cirrus (see section 3a) and therefore underestimates the total εN.

For low-level clouds, having a small radiative effect in the LW, 3I- and ISCCP-sampled OLRs agree well. In both cases, the OLR is larger for single-layer clouds than for multilayer clouds, as one would expect.

In Figs. 20a–f, one observes a strong increase of FSW with εN; the largest values are produced by high opaque clouds, followed by midlevel and then by low-level opaque clouds. Heterogeneities play a much more important role in the SW radiative flux when sampling according to IR or VIS radiances. Considering Figs. 20g–i, we find this time that for transmissive clouds ($\varepsilon N < 0.9$) $\mathrm{FSW}_{ERBE}(\varepsilon N_{3I}) > \mathrm{FSW}_{ERBE}(\varepsilon N_{ISCCP})$, if $\varepsilon N_{3I} = \varepsilon N_{ISCCP}$ for heterogeneous single-layer and multilayer clouds, but $\mathrm{FSW}_{ERBE}(\varepsilon N_{3I}) < \mathrm{FSW}_{ERBE}(\varepsilon N_{ISCCP})$, if $\varepsilon N_{3I} = \varepsilon N_{ISCCP}$ for homogeneous single-layer low-level clouds. The latter case can be explained by an overestimation of εN for homogeneous single-layer low-level clouds by 3I for broken clouds with element sizes smaller than the HIRS pixels.

For horizontally as well as vertical heterogeneous clouds εN obtained from averaged IR radiances characterizes a more reflective scene than the same εN obtained from sampled VIS radiances.

5. Conclusions

Small-scale heterogeneities, both horizontal and vertical, play an important role in determining the relationship between cloud information obtained from satellite IR sounders (3I) and imagers also using VIS radiance measurements (ISCCP). The effective cloud amount as calculated by 3I agrees quite well with that obtained by ISCCP for homogeneous clouds with uniform properties over a 1° area. Heterogeneities in cloud properties lead to a smaller 3I effective cloud amount. When cirrus overlie low-level clouds, the IR sounder-derived cloud properties are dominated by the properties of the uppermost cloud, whereas the visible radiance measurements used by ISCCP include, and may be dominated by, the properties of the lowermost cloud layer, producing a larger effective cloud amount for ISCCP. Hence, combined use of the 3I-retrieved effective cirrus emissivity and visible information gives the opportunity to distinguish single-layer cirrus from cirrus overlying thicker clouds.

Cloud-induced LW flux changes produce a warming of the earth and vary between 0 and 150 W m^{-2}, depending on cloud type and cover, as well as on clear sky atmospheric conditions. The improvement of cirrus identification in the reprocessed ISCCP dataset leads to a better distinction of their cloud radiative effects, in better agreement with 3I. Cloud-induced SW flux changes produce a cooling of the earth that depends very strongly on the solar inclination as well as on cloud optical thickness and cover. The net radiative effect (LW and SW) of thin cirrus is very small, similar to that of partial cover by low-level clouds; however, their separate warming and cooling effects are larger. The subtle dependence of the differences between the 3I and ISCCP cloud-type parameters and their associated radiative effects on small-scale (<100 km) horizontal and vertical cloud heterogeneities arises from differences in averaging IR or VIS radiances. More extensive studies, including other datasets, for example from the Tropical Rainfall Measuring Mission, to help separate different microphysics and vertical layering, will certainly give more insight to these problems.

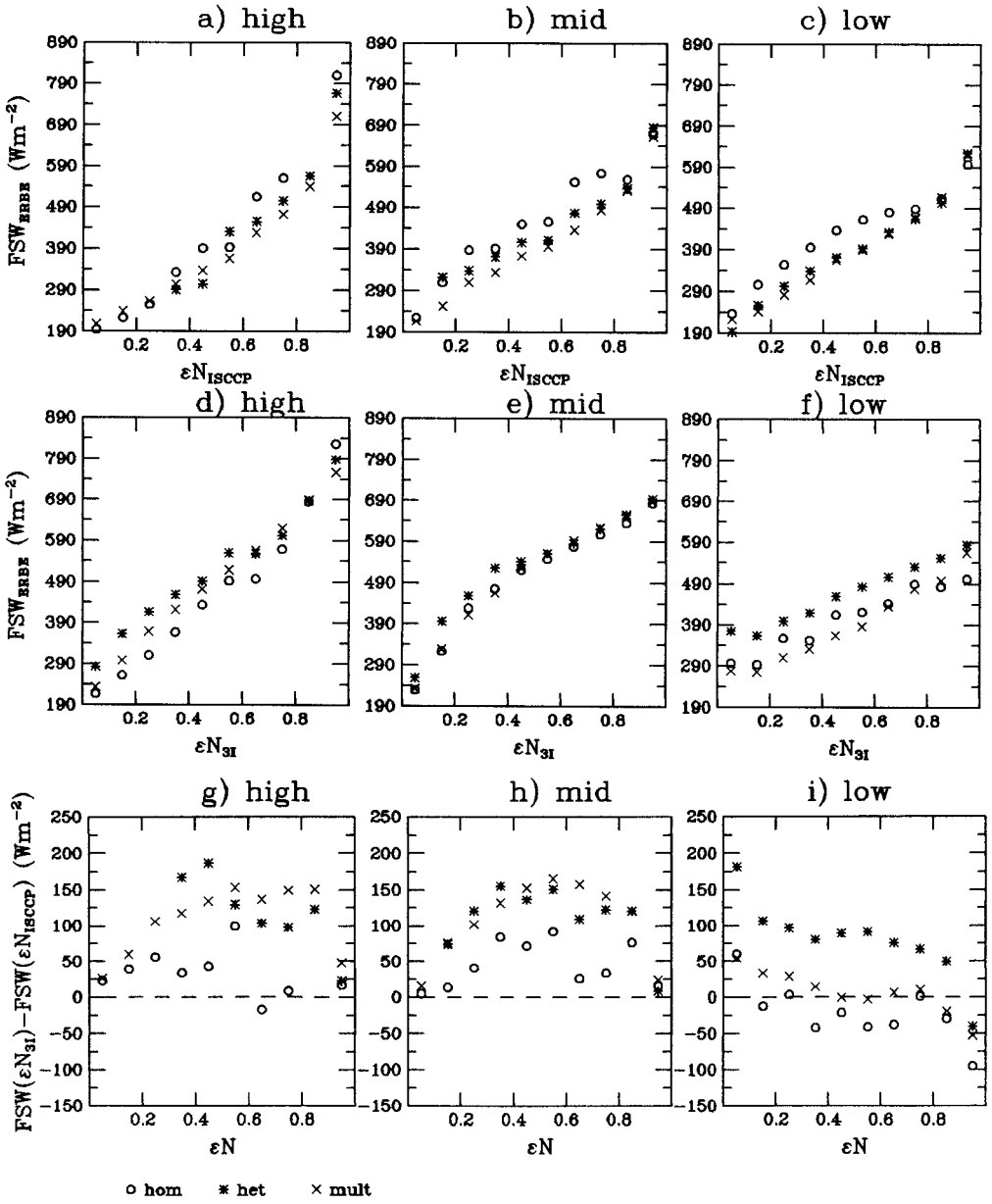

FIG. 20. (a)–(f) ERBE-reflected SW flux, (divided by $\cos\theta_0$), as a function of effective cloud amount as determined by ISCCP (a)–(c) and by 3I (d)–(f), respectively, for high- (a), (d), mid- (b), (e) and low-level clouds (c), (f). For each cloud-height type, homogeneous (○) and heterogeneous one-layer clouds (*) as well as multilayer clouds (×) are considered. Observations are averaged over ocean between 30° and 60°N in Jul 1987. (g)–(i) Difference between ERBE-reflected SW flux (divided by $\cos\theta_0$), sampled as a function of 3I and ISCCP effective cloud amount for high- (g), mid- (h), and low-level clouds (i).

Acknowledgments. Special thanks to Alison Walker at NASA/GISS, who made it possible to become acquainted with the details of the ISCCP data, and to Jeff Jonas at NASA/GISS who helped with graphics support. The 3I processing was performed on the computers of the Institut du Développement et des Ressources en Informatique Scientifique of the Centre National de la Recherche Scientifique.

APPENDIX

Averaging τ and ε

To determine the cloud optical thickness, τ, for each cloudy pixel, the ISCCP analysis compares the observed reflected radiance to lookup tables representing the results of offline radiative transfer calculations that account for full multiple scattering within the cloud and

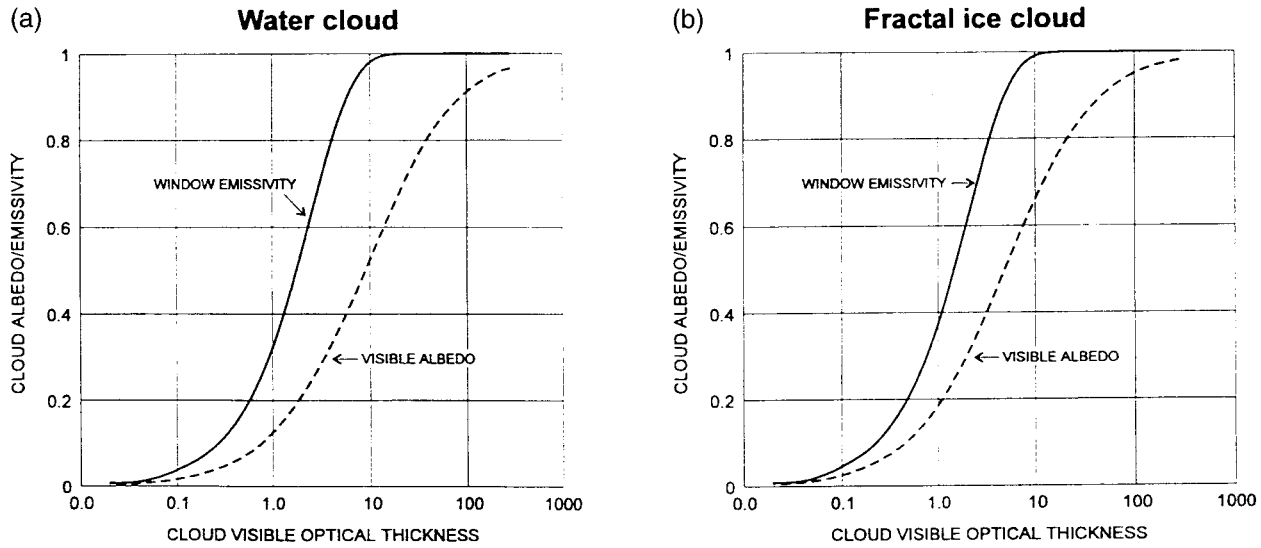

FIG. A1. Relations of cloud visible (0.6 μm) albedo (scene albedo over black surface with no atmosphere) and infrared (10.5 μm) emissivity as a function of optical depth at 0.6 μm for the liquid (left) and ice (right) water cloud models used in the ISCCP radiative analysis (from Rossow et al. 1996)

among the cloud, atmosphere, and surface as a function of viewing and illumination geometry. This relationship is shown in Fig. A1 (from Fig. 3.13 in Rossow et al. 1996). In order to start with a simple relationship between optical thickness and radiance, for a mathematical illustration and definition of the averaging procedures, we express the cloud optical thickness as a function of incident (I_0) and transmitted radiance (I_t):

$$\tau = \ln(I_0/I_t). \tag{A1}$$

There are three methods to calculate the average IR cloud emissivity from ISCCP at a spatial resolution of 1°.

1) The first method, which is equivalent to that used by 3I, consists of transforming τ of each cloudy pixel into ε by Eq. (4), and then averaging the IR cloud emissivities over the cloudy pixels inside the 1° grid:

$$\overline{\varepsilon} = 1 - \frac{1}{N}\sum_{j=1}^{N} \exp\left[-\left(\ln\frac{I_0}{I_t^j}\right)\Big/ b\right]$$

$$= 1 - \left(\frac{1}{I_0}\right)^{1/b}\frac{1}{N}\sum_{j=1}^{N}(I_t^j)^{1/b}. \tag{A2}$$

2) The second method is used in the ISCCP processing to give average cloud optical thicknesses over

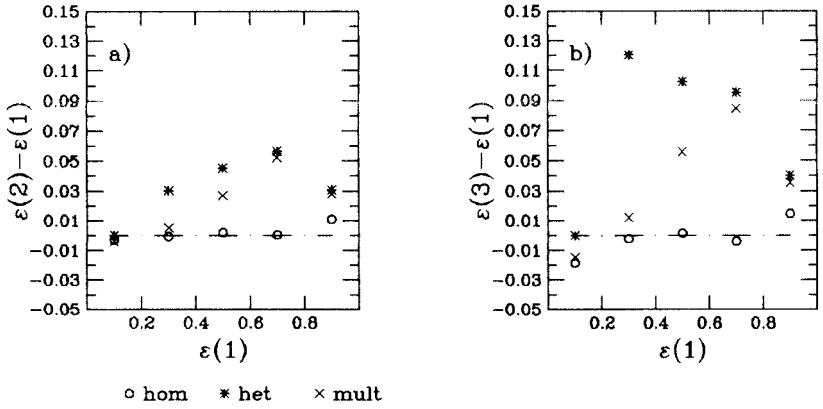

FIG. A2. (a) Difference of ISCCP-averaged cloud emissivities ε determined from method 2 and from method 1 as a function of ISCCP-averaged cloud emissivity ε as obtained by method 1, and (b) difference of ISCCP-averaged cloud emissivities ε determined from method 3 and from method 1 as a function of ISCCP-averaged cloud emissivity ε as obtained by method 1. Three spatial heterogeneity situations over the 1° grids are shown: ○ homogeneous, same ISCCP cloud type over 1° grid; * same ISCCP cloud height but heterogeneous optical thickness; and × multilayer; different ISCCP cloud heights and optical thicknesses. Data are analyzed over the NA in Jul 1987.

$2.5° \times 2.5°$ areas (D1 and D2 data) that preserve average cloud albedos (Rossow et al. 1996). The calculated VIS transmittances, I_0/I_t, are averaged over the cloudy pixels within the area and then transformed into an average τ by the lookup table. Finally, one can apply Eq. (4) to obtain the average IR cloud emissivity:

$$\varepsilon[\tau(\overline{I}_t)] = 1 - \exp\left[-\ln\left(\frac{I_0}{\frac{1}{N}\sum_{j=1}^{N} I_t^j}\right)\Big/ b\right]$$

$$= 1 - \left(\frac{\frac{1}{N}\sum_{j=1}^{N} I_t^j}{I_0}\right)^{1/b}$$

$$= 1 - \left(\frac{1}{I_0}\right)^{1/b}\left[\frac{1}{N}\sum_{j=1}^{N} (I_t^j)\right]^{1/b}. \quad \text{(A3)}$$

3) In the third method, τ is averaged directly over the cloudy pixels within the area. This average represents what a GCM will predict from its cloud water parametrization (viz., area-average cloud water content) and is used in studies of cloud heterogeneity effects on radiation as the so-called plane-parallel cloud (e.g., Cahalan et al. 1994). Then applying Eq. (4), the average IR cloud emissivity is

$$\varepsilon(\overline{\tau}) = 1 - \exp\left(-\frac{1}{N}\sum_{j=1}^{N} \tau_j/b\right)$$

$$= 1 - \exp\left[-\frac{1}{N}\sum_{j=1}^{N} \ln\left(\frac{I_0}{I_t^j}\right)\Big/ b\right]$$

$$= 1 - \exp\left[-\frac{\ln I_0}{b} + \frac{1}{N \times b}\sum_{j=1}^{N} \ln(I_t^j)\right]$$

$$= 1 - \left(\frac{1}{I_0}\right)^{1/b} \prod_{j=1}^{N} (I_t^j)^{1/(N\times b)}. \quad \text{(A4)}$$

Figure A2a shows the difference between ε calculated from method 2 and ε from method 1 as a function of ε from method 1 under the three heterogeneity conditions described in section 3a. Both methods yield the same result in the case of homogeneous cloud situations, but when heterogeneities appear, the IR cloud emissivity calculated by method 2 exceeds the one obtained by method 1 on the average by about 10%, with the exception of emissivities near 1, where both methods yield again similar results, due to saturation. By averaging over all IR cloud emissivities within one cloud-type height (separately for high-, mid-, and low-level clouds), the effect is reduced to about 5% (not shown). Method 3 yields even larger emissivities than method 2, as shown in Fig. A2b.

For an illustration we imagine the following example: A thin cloud, covering two pixels with $\tau_1 = 0.2$ and $\tau_2 = 0.4$, and a thick cloud, covering two pixels with $\tau_3 = 1$ and $\tau_4 = 20$, are within the same 1° grid. We calculate the average IR cloud emissivity ε of the thin cloud, of the thick cloud, and of the combination of the two clouds by using methods 1–3. For the thin cloud, the results (0.27, 0.28, and 0.28) do not differ, because the pixel optical thicknesses do not differ much. For the thick cloud, methods 1–3 yield 0.83, 1.00, and 1.00. In this case, the last two methods come to saturation, whereas the first method gives a lower average IR emissivity. The largest variation in the results appears when mixing thick and thin clouds: the average 1° grid IR cloud emissivities are then 0.55, 0.91, and 1.0.

REFERENCES

Ackerman, S. A., R. A. Frey, and W. L. Smith, 1992: Radiation budget studies using collocated observations from Advanced Very High Resolution Radiometer, High-Resolution Infrared Sounder/2, and Earth Radiation Budget Experiment instruments. *J. Geophys. Res.,* **97,** 11 513–11 25.

Armante, R., L. Crépeau, N. A. Scott, and A. Chédin, 1998: Correction for spurious trends in the 3I reanalysis of TOVS data. Preprints, *Ninth Conf. on Satellite Meteorolgy and Oceanography*, Vol. 2, Paris, France, Amer. Meteor. Soc., 718–720.

Barksrom, B. R., E. F. Harrison, G. L. Smith, R. Green, J. Kibler, R. Cess, and the ERBE Science Team, 1989: Earth Radiation Budget Experiment (ERBE) archival and April 1985 results. *Bull. Amer. Meteor. Soc.,* **70,** 1254–1262.

Baum, B. A., R. F. Arduini, B. Wielicki, P. Minnis, and S.-Ch. Tsay, 1994: Multilevel cloud retieval using multispectral HIRS and AVHRR data: Nighttime oceanic analysis. *J. Geophys. Res.,* **99,** 5499–5514.

Cahalan, R. F., W. Ridgeway, W. J. Wiscombe, T. L. Bell, and J. B. Snider, 1994: The albedo of fractal stratocumulus clouds. *J. Atmos. Sci.,* **51,** 2434–2455.

Chaboureau, J.-P., A. Chédin, and N. A. Scott, 1998: Remote sensing of the vertical distribution of atmospheric water vapor from the TOVS observations. Method and validation. *J. Geophys. Res.,* **103,** 8743–8752.

Chédin, A., N. A. Scott, C. Wahiche, and P. Moulinier, 1985: The improved initialized inversion method: A high resolution physical method for temperature retrievals from the TOVS-N series. *J. Climate Appl. Meteor.,* **24,** 124–143.

Del Genio, A. D., W. Kovari, and K.-W. Lo, 1996: A prognostic cloud water parametrization for global climate models. *J. Climate,* **9,** 270–304.

Eyre, J. R., and W. P. Menzel, 1989: Retrieval of cloud parameters from satellite sounder data: A simulation study. *J. Appl. Meteor.,* **28,** 267–275.

Jin, Y., and W. B. Rossow, 1997: Detection of cirrus overlapping low-level clouds. *J. Geophys. Res.,* **102,** 1727–1737.

Liao, X., W. B. Rossow, and D. Rind, 1995: Comparison between SAGE II and ISCCP high-level coulds. Part II: Locating cloud tops. *J. Geophys. Res.,* **100,** 1137–1147.

Minnis, P., P. W. Heck, and D. F. Young, 1993: Inference of cirrus cloud properties using satellite-observed visible and infrared radiances. Part II: Verification of theoretical cirrus radiative properties. *J. Atmos. Sci.,* **50,** 1305–1322.

Ramanathan, V., R. D. Cess, E. F. Harrison, P. Minnis, B. R. Barkstrom, E. Ahmad, and D. Hartmann, 1989: Radiative cloud forcing and climate: Results from the Earth Radiation Budget Experiment. *Science,* **243,** 57–63.

Rossow, W. B., and R. A. Schiffer, 1991: ISCCP cloud data products. *Bull. Amer. Meteor. Soc.,* **72,** 1–20.

——, and Y.-C. Zhang, 1995: Calculation of surface and top of atmosphere radiative fluxes from physical quantities based on

ISCCP data sets. 2. Validation and first results. *J. Geophys. Res.*, **100,** 1167–1197.

——, A. W. Walker, and L. C. Garder, 1993: Comparison of ISCCP and other cloud amounts. *J. Climate,* **6,** 2394–2418.

——, ——, D. Beuschel, and M. Roiter, 1996: International Satellite Cloud Climatology Project (ISCCP): Description of new cloud datasets. WMO/TD-737, World Climate Research Programme (ICSU and WMO), Geneva, Switzerland, 115 pp.

Scott, N. A., and Coauthors, 1999: Characteristics of the TOVS Pathfinder Path-B Dataset. *Bull. Amer. Meteor. Soc.,* in press.

Sèze, G., and W. B. Rossow, 1991: Effects of satellite data resolution on measuring the space/time variations of surfaces and clouds. *Int. J. Remote Sens.,* **12,** 921–952.

Smith, W. L., H. M. Woolf, M. C. Hayden, D. Q. Wark, and L. M. McMillin, 1979: The TIROS-N Operational Vertical Sounder. *Bull. Amer. Meteor. Soc.,* **60,** 1177–1187.

Stephens, G. L., and T. J. Greenwald, 1991: The earth's radiation budget and its relation to atmospheric hydrology. 2. Observations of cloud effects. *J. Geophys. Res.,* **96,** 15 325–15 340.

Stubenrauch, C. J., 1993: Collocation of AVHRR, ERBE and HIRS/MSU data. Laboratoire de Météorologie Dynamique, Internal Note 185, 9 pp.

——, A. D. Del Genio, and W. B. Rossow, 1997: Implementation of sub-grid cloud vertical structure inside a GCM and its effect on the radiation budget. *J. Climate,* **10,** 273–287.

——, A. Chédin, R. Armante, and N. A. Scott, 1999a: Clouds as seen by satellite sounders (3I) and imagers (ISCCP). Part II: A new approach for cloud parameter determination in the 3I algorithms. *J. Climate,* **12,** 2214–2223.

——, R. Holz, A. Chédin, D. L. Mitchell, and A. Baran, 1999b: Retrieval of cirrus ice crystal sizes from 8.3 and 11.1 μm emissivities determined by the improved initialization inversion of TIROS-N Operational Vertical Sounder observations. *J. Geophys. Res.,* in press.

——, W. B. Rossow, F. Chéruy, A. Chédin, and N. A. Scott, 1999c: Clouds as seen by satellite sounders (3I) and imagers (ISCCP). Part I: Evaluation of cloud parameters. *J. Climate,* **12,** 2189–2213.

Thomas, D., J. Ph. Duvel, and R. S. Kandel, 1995: Diurnal bias in calibration of broad-band radiance measurements from space. *IEEE Trans. Geosci. Remote Sens.,* **33,** 670–683.

Warren, S. G., C. J. Hahn, and J. London, 1985: Simultaneous occurrence of different cloud types. *J. Climate Appl. Meteor.,* **24,** 658–667.

Wielicki, B. A., and L. Parker, 1992: On the determination of cloud cover from satellite sensors: The effect of sensor spatial resolution. *J. Geophys. Res.,* **97,** 12 799–12 823.